Energy Conversion and Management 368 (2026) 122019

Contents lists available at ScienceDirect

Energy Conversion and Management

journal homepage: www.elsevier.com/locate/enconman

Research Paper

Thermal-Mechanical fatigue and creep damage characteristics of an efficient and responsive supercritical CO_2 cooling wall

Ting Zhao, Yanjuan Wang *, Xuan Xu, Junhao Cui, Binhui Yu, Jinliang Xu

The Beijing Key Laboratory of Multiphase Flow and Heat Transfer, North China Electric Power University, Beijing 102206, China

ARTICLE INFO

Keywords:
Supercritical carbon dioxide
load change rate
coal-fired power generation
fatigue damage
creepdamage

ABSTRACT

The supercritical carbon dioxide (S-CO_2) coal-fired power plant is a significant way to improve the efficiency and realize the rapid peaking of coal-fired power generation. However, under rapid peaking conditions, the S-CO_2 cooling wall experiences significant creep and fatigue damage. This study presents a comprehensive characterization of cooling wall tubes during variable load peaking operations. A steady-state multi-physics coupling model for the S-CO_2 cooling wall and a transient damage model under variable load conditions were developed. Model validation was performed using experimental S-CO_2 turbulent heat transfer data and theoretical analysis. The variations in temperature, stress, and damage of the cooling wall under both steady-state and transient variable-load conditions were obtained. A sensitivity analysis was conducted to evaluate the influence of key operating parameters on cooling wall tube performance. The influence of load change rate on cooling wall tube damage was investigated. An optimization strategy was proposed to match the load change rate with the system load. Compared to the constant rate strategy, the new method effectively reduces the cooling wall's temperature rise rate. During the load-increasing process, it achieves maximum reductions of 10.51 K in temperature and 21.53 MPa in stress, while reducing maximum creep damage by 37.56% and maximum fatigue damage by 27.45%. This strategy enhances the flexibility and safety of the cooling wall, offering theoretical support for the design of high-efficiency, flexible S-CO_2 cooling walls under transient variable-load conditions.

1. Introduction

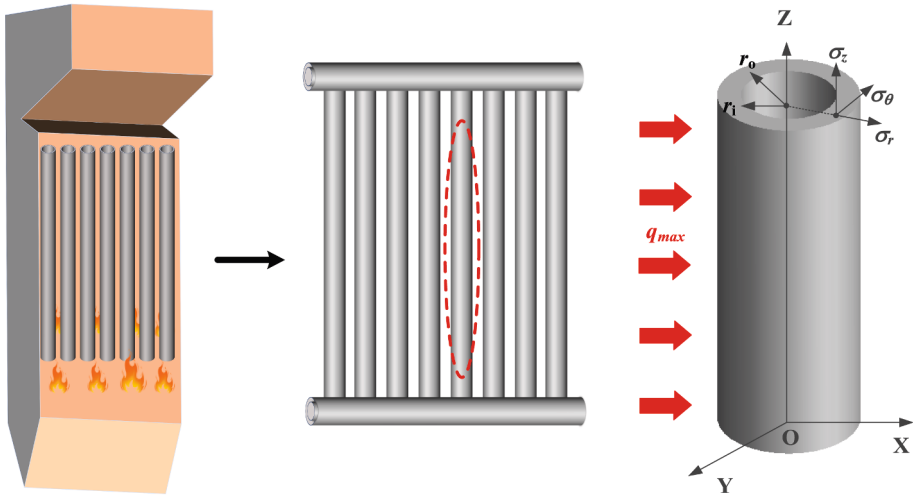
The increasing integration of renewable energy into power grids presents growing challenges to system stability. Power systems need a higher level of flexibility to accommodate intermittent renewable energy [1]. Currently, coal-fired power plants represent the dominant power source in China. However, power generation units primarily relying on steam Rankine cycles face technical bottlenecks in both improving power generation efficiency and enhancing operational flexibility. Transformative innovations are therefore urgently required to address these challenges.

Supercritical carbon dioxide (S-CO_2) cycles have the advantages of high efficiency [2,3], excellent flexibility [4], compact layout [5] and various heat sources adaptability [6]. Owing to the system's low volumetric and thermal inertia, it offers strong potential for deep and rapid load regulation. Accordingly, the S-CO_2 cycle is widely regarded as a promising alternative to the conventional steam Rankine cycle, capable of improving the load-following rate of coal-fired power units. The key components, including S-CO_2 turbines and compressors, are approximately one-tenth the size of their counterparts in steam cycle. It is projected to achieve a load regulation range of 10%-100% at a rate of 6% /min [7]. Consequently, the S-CO_2 coal-fired power generation systems show considerable potential for enhancing the operational flexibility of coal-fired units [8].

As a critical component of S-CO_2 coal-fired power systems, S-CO_2 boilers have attracted significant research attention from scholars worldwide in recent years. While the high efficiency and operational flexibility of the S-CO_2 power cycle enable rapid load-following, they also induce rapid fluctuations in temperature and stress within the boiler's heating surfaces, especially in the cooling walls. Operating under conditions of high temperature, high pressure, and high non-uniform heat flux (NUH), the cooling walls represent vulnerable components of the S-CO_2 boiler, posing significant challenges to system safety [9]. Yang et al. [10] conducted coupled combustion and heat transfer simulations for a 300 MW S-CO_2 boiler. Their methodology integrated a three-dimensional model of in-furnace combustion with a one-dimensional simulation of flow and heat transfer within the cooling wall tubes, thereby deriving a one-dimensional temperature distribution

* Corresponding author.
E-mail address: 90102184@ncepu.edu.cn (Y. Wang).

https://doi.org/10.1016/j.enconman.2026.122019
Received 25 May 2026; Received in revised form 30 July 2026; Accepted 2 August 2026
Available online 7 August 2026
0196-8904/© 2026 Published by Elsevier Ltd.



(a) S-CO_2 boiler (b) Physical model.

Fig. 1. Schematic of cooling wall tube in S-CO_2 boiler.

along the walls. Zhou et al. [11] developed a one-dimensional mathematical model to simulate flow and heat transfer in the cooling walls of a 1000 MW S-CO_2 boiler. They obtained the temperature and pressure drop distributions along the cooling walls and proposed three optimization strategies: a split-flow configuration, a symmetrical flow arrangement, and a localized boiler expansion design. The results demonstrated that reducing tube diameter and wall heat flux effectively lowers wall temperatures. Additionally, the pressure drop decreases exponentially as flow splits increase. Zhou et al. [12]investigated the effect of flue gas recirculation on the temperature of cooling walls. Their results demonstrated that recirculating flue gas into the furnace significantly reduces the furnace heat flux, thereby lowering cooling wall temperatures. However, relying exclusively on flue gas recirculation may compromise combustion performance. They proposed "partial expansion in the upper zone +double furnace + symmetry flow mode" boiler design, which effectively lowers cooling wall temperatures while maintaining combustion stability and limiting the maximum wall temperature to below 943 K. To mitigate excessively high temperatures in S-CO_2 boiler cooling walls, Liu et al. [9] developed a one-dimensional steady-state model for flow and heat transfer across the entire cooling wall system. Through the sequential implementation of four technical measures: improving lateral furnace coupling, adopting flue gas recirculation to reduce heat flux, enhancing vertical furnace coupling, and intensifying in-tube heat transfer, they successfully lowered the cooling wall temperature from 943.65 K to 908.15 K. The aforementioned studies have predominantly focused on steady-state heat transfer processes within S-CO_2 cooling walls. However, the thermo-mechanical coupling behavior induced by abrupt temperature and stress fluctuations during rapid load transients has not been elucidated. This behavior is of critical importance to the structural integrity and service life of the cooling walls.

During rapid load-following transients, abrupt temperature changes in boiler cooling walls induce thermal and mechanical stress shocks, resulting in fatigue damage. Moreover, prolonged exposure to high temperature, high pressure, and NUH results in creep damage and other safety concerns. A thorough investigation of the integrated thermo-mechanical characteristics of S-CO_2 coal-fired boiler cooling walls under transient load-varying conditions is imperative to ensure operational safety. Nevertheless, research on the combined fatigue-creep behavior of S-CO_2 cooling walls during rapid transients remains remarkably scarce. S-CO_2 solar tower receivers encounter similarly severe operating environments, characterized by high temperatures, high pressures, and NUH. Therefore, findings from solar receiver studies can serve as a valuable reference for analyzing the transient thermo-mechanical behavior of cooling walls.

To address thermal stress and fatigue failure caused by frequent cold starts in receivers, Wan et al. [13] developed a coupled model integrating optical propagation, photothermal conversion, thermo-elasticity, and fatigue assessment. Their simulation provided the radial, circumferential, and axial stress distributions in the S-CO_2 receiver tube. The results indicated that high temperature and NUH lead to significant thermal stress and deformation in the receiver, with stress concentration most pronounced in welded regions. The study also highlighted the considerable impact of weld quality on fatigue failure. For a single receiver tube, Chen et al. [14] applied the Linear Damage Accumulation (LDA) theory, the Manson-Coffin formula and the Mendelson-Robertson-Manson (M-R-M) relation to analyze the effects of key parameters such as mass flow rate (0.25-2.5 kg/s), wall thickness (0.25-2 mm), and tube diameter (3-18 mm) on fatigue-creep damage. Their findings show that creep damage exceeds fatigue damage. As the tube diameter increases from 3 mm to 18 mm, the maximum inner wall temperature and equivalent stress rise rapidly, leading to increased damage. Reducing the tube diameter effectively mitigates fatigue-creep damage in the receiver tube. Nithyanandam et al. [15] conducted a study on the thermo-structural and fatigue-creep characteristics of a single S-CO_2 receiver tube, investigating the effects of geometric and operational parameters on thermal efficiency, thermal stress, and creep-fatigue life. They found that while smaller tube diameters and higher heat flux can improve thermal efficiency, these also lead to increased pressure drop. It should be noted that their thermal model did not account for circumferential non-uniformity in heat flux or the life reduction caused by the interaction between creep and fatigue damage. Ortega et al. [16]developed a three-dimensional model of an S-CO_2 receiver under NUH, analyzing heat transfer and fatigue-creep damage. The study evaluated the feasibility and safety margin of Inconel 625 under conditions of 20 MPa and 973 K. Within a temperature range of 933.15-1093.15K and at 20 MPa, fatigue damage was found to be significantly lower than creep damage. Current knowledge on fatigue damage in tower–type S–CO_2 solar receivers is largely confined to linear damage accumulation rules, and their creep–fatigue coupled assessment has laid a groundwork for transient analyses of cooling walls. Nevertheless, the cooling walls of large coal–fired boilers are markedly distinct

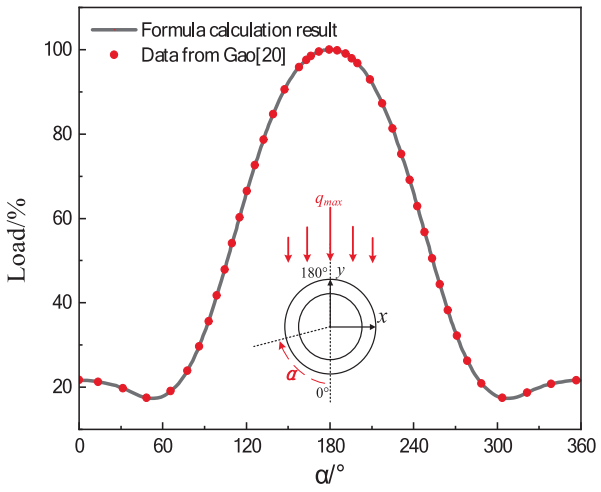


Fig. 2. Non-uniform heat flux distribution

from solar receivers in geometry and operating conditions.

To address these research gaps and elucidate the thermomechanical damage mechanisms in the cooling walls of S-CO_2 coal-fired boilers under transient conditions, this study presents the following contributions:

1. A steady-state three-dimensional multi-physics coupling model for the S-CO_2 cooling wall and a transient damage model under variable load conditions were developed. The validity of the model was verified through experimental data and theoretical analysis. The dynamic variations in temperature, stress, and damage of the cooling wall were obtained.
2. A sensitivity analysis was conducted to evaluate the influence of key operating parameters on cooling wall tube performance. The effect of load change rate on the integrated thermo-mechanical behavior of cooling wall tubes during transient operation was investigated.
3. An optimization strategy was proposed to match the load change rate with the system load, wherein a quadratic function was used to define the load change rate. This provides a theoretical basis for the optimized design of efficient and flexible S-CO_2 cooling walls under transient operating conditions.

Numerical model and method

Physical model

Fig. 1 shows the schematic of an S-CO_2 cooling wall, where each tube connects independently to upper and lower headers. Given the geometric complexity of the full cooling wall panel and the similarity of heat flux distribution among individual tubes, a 1-meter single tube was selected as the representative physical model to reduce computational cost while preserving the essential physics. The tube is made of Inconel 625, with an outer radius (R) of 45 mm and an inner radius (r) of 30 mm. Gravity is contrary to the S-CO_2 flow direction. A circumferential NUH [17] was applied on the outer tube wall, as shown in Fig. 2, the heat flux peaks at a circumferential angle of $\alpha = 180°$. Its minima occur at about $\alpha = 51.5°$ and $\alpha = 308.5°$, attributable to wall-reflected radiation.

2.2. Governing equations

A three-dimensional steady-state cooling wall tubes model with coupled hydrodynamics, thermodynamics, and solid mechanics was developed, incorporating variations in S-CO_2 thermophysical parameters from NIST [18].

The Reynolds number for S-CO_2 within the tubes is approximately 3.6×10^5, indicating turbulent flow, so the k-ε turbulence model with the wall function was employed to describe the flow and heat transfer processes of S-CO_2 within the cooling walls. The characteristics of the cooling wall are governed by the continuity equation, energy equation, and momentum equation, which are as follows: [19].

Continuity equation:

$$\frac{\partial}{\partial x_i}(\rho u_i) = 0 \tag{1}$$

Energy equation:

$$\rho C_p u_i \frac{\partial T}{\partial x_i} = (\lambda + \lambda_T)\frac{\partial}{\partial x_i}(\frac{\partial T}{\partial x_i}) + Q \tag{2}$$

Momentum equation:

$$\frac{\partial}{\partial x_j}(\rho u_i u_j) = -\frac{\partial p}{\partial x_i} + \frac{\partial}{\partial x_j}[(\mu+\mu_t)(\frac{\partial u_i}{\partial x_j}+\frac{\partial u_j}{\partial x_i}) - \frac{2}{3}(\mu+\mu_t)\frac{\partial u_i}{\partial x_i}\delta_{ij} - \frac{2}{3}\rho k\delta_{ij}] \tag{3}$$

The turbulent viscosity (in the k-ε model), defined as follows:

$$\mu_t = \rho C_\mu \frac{k^2}{\varepsilon} \tag{4}$$

The transport equations for k and turbulent dissipation rate ε are as follows:

$$\frac{\partial \rho k}{\partial t} + U_j\frac{\partial \rho k}{\partial x_j} = \tau_{ij}\frac{\partial U_i}{\partial x_j} - \rho\varepsilon + \frac{\partial}{\partial x_j}\left[\left(\mu + \frac{\mu_t}{\sigma_k}\right)\frac{\partial k}{\partial x_j}\right] \tag{5}$$

$$\frac{\partial \rho \varepsilon}{\partial t} + U_j\frac{\partial \rho \varepsilon}{\partial x_j} = C_{\varepsilon 1}\frac{\varepsilon}{k}\tau_{ij}\frac{\partial U_i}{\partial x_j} - C_{\varepsilon 2}\rho\frac{\varepsilon^2}{k} + \frac{\partial}{\partial x_j}\left[\left(\mu + \frac{\mu_t}{\sigma_\varepsilon}\right)\frac{\partial \varepsilon}{\partial x_j}\right] \tag{6}$$

where $C_{\varepsilon 1}$=1.44,$C_{\varepsilon 2}$=1.92,σ_k=1.0,σ_ε=1.3,C_μ=0.09.

The heat transfer process occurs within the cooling tube wall, described by the following equation:

$$\frac{\partial^2 T_s}{\partial x^2} + \frac{\partial^2 T_s}{\partial y^2} + \frac{\partial^2 T_s}{\partial z^2} = 0 \tag{7}$$

The heat transfer between the pipe wall and S-CO_2 is calculated using the "heat wall function". The corresponding heat flux at the fluid-solid interface is defined as:

$$Q = \frac{\rho C_P u_\tau (T_w - T_f)}{T^+} \tag{8}$$

where the subscripts i and j are equal to values of 1, 2 and 3, which stand for the corresponding directions of the x, y and z; Unlike a third-order tensor which would require an additional index k, the present formulation concerns only second-order tensor components. u represents the velocity vector; ρ is the density; T stands for the temperature; Cp is the specific heat capacity at constant pressure; p is the pressure; μ is the dynamic viscosity; μ_t stands for the turbulent viscosity; Pr is the Prandtl number; Prt represents the Prandtl number for thermal diffusion; g is the gravitational acceleration.

2.2.1. Stress model

The inner surface of cooling wall tube operates under high pressure which induces mechanical stress. Simultaneously, the outer surface of cooling wall tube is subjected to highly NUH which creates a steep temperature gradient in the tube and results in thermal stress.

Thermal stress is calculated as follows [20]:

$$\sigma_r = \frac{\alpha E \Delta T_r}{2(1-\nu)\ln(r_o/r_i)}\left[-\ln\frac{r_o}{r} - \frac{r_i^2}{(r_o^2-r_i^2)}\left(1-\frac{r_o^2}{r^2}\right)\ln\frac{r_o}{r_i}\right] \tag{9}$$

$$\sigma_z = \frac{\alpha E \Delta T_r}{2(1-\nu)\ln(r_o/r_i)}\left[1 - 2\ln\frac{r_o}{r} - \frac{2r_i^2}{(r_o^2-r_i^2)}\ln\frac{r_o}{r_i}\right] \tag{10}$$

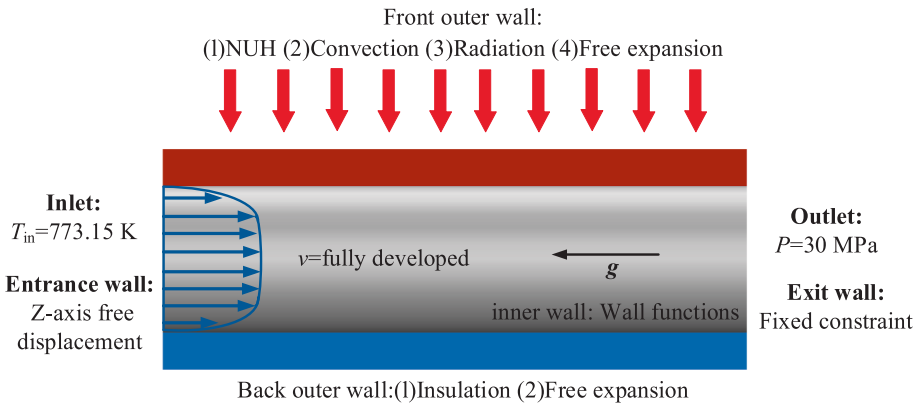


Fig. 3. Detailed boundary conditions

Table 1
Fatigue-creep coefficients for Inconel 625 steel. [22]

Model	Constant				
Basquin &	T/K	σ'_f/MPa	c_1	ε'_f /%	c_2
Coffin-Mason	298.15	2263.7	-0.142	0.97	-0.597
	923.15	983.8	-0.082	0.32	-0.595
	1033.15	895.7	-0.072	1.56	-0.963
Norton	A_c/s^{-1}	n_c	Q_c/kJ·mol^{-1}	σ_{ref}/MPa	T_{ref} /K
	6.78·10^{-95}	13.37	447	1	898.15
M-R-M	β_0	β_1	β_2	β_3	
	-44.2641	65825	12.2	- 20289	
	T/K	K'/MPa	n'		
	923.15	1492.7	0.17		
	1033.15	796.4	0.066		

$$\sigma_\theta = \frac{\alpha E \Delta T_r}{2(1-\nu)\ln(r_o/r_i)}\left[1 - \ln\frac{r_o}{r} - \frac{r_i^2}{(r_o^2 - r_i^2)}\left(1 + \frac{r_o^2}{r^2}\right)\ln\frac{r_o}{r_i}\right] \tag{11}$$

The pressure stress can be calculated by Eq. (12) to Eq. (14), as follows:

$$\sigma_E^{P_r} = \frac{P_i r_i^2}{r_o^2 - r_i^2}\left(1 - \frac{r_o^2}{r^2}\right) \tag{12}$$

$$\sigma_E^{P_\theta} = \frac{P_i r_i^2}{r_o^2 - r_i^2}\left(1 + \frac{r_o^2}{r^2}\right) \tag{13}$$

$$\sigma_E^{P_z} = \frac{P_i r_i^2}{r_o^2 - r_i^2} \tag{14}$$

The total stress components are calculated as follows:

$$\sigma_i^E = \sigma_{T,i}^E + \sigma_{P,i}^E i = r, \theta, z \tag{15}$$

The elastic strain is calculated according to Hooke's law:

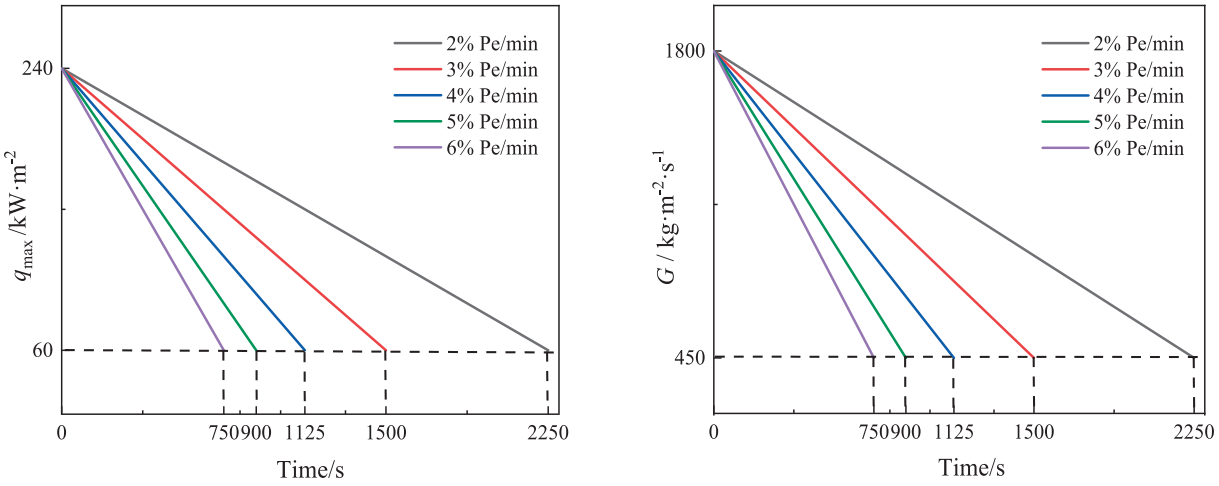
$$\varepsilon_E^1 = \frac{1}{E}\left[\sigma_E^1 - \nu\left(\sigma_E^2 + \sigma_E^3\right)\right] + \alpha T \tag{16}$$

$$\varepsilon_E^2 = \frac{1}{E}\left[\sigma_E^2 - \nu\left(\sigma_E^1 + \sigma_E^3\right)\right] + \alpha T \tag{17}$$

$$\varepsilon_E^3 = \frac{1}{E}\left[\sigma_E^3 - \nu\left(\sigma_E^2 + \sigma_E^1\right)\right] + \alpha T \tag{18}$$

According to the von-Mises equivalent stress theory [21], The equivalent elastic stress and strain are calculated as follows:

$$\sigma_E^{eq} = \sqrt{\frac{1}{2}\left[\left(\sigma_E^1 - \sigma_E^2\right)^2 + \left(\sigma_E^2 - \sigma_E^3\right)^2 + \left(\sigma_E^3 - \sigma_E^1\right)^2\right]} \tag{19}$$



(a) heat flux density (b) mass flux

Fig. 4. Parameter variations during the load reduction process from 100% to 25% load.

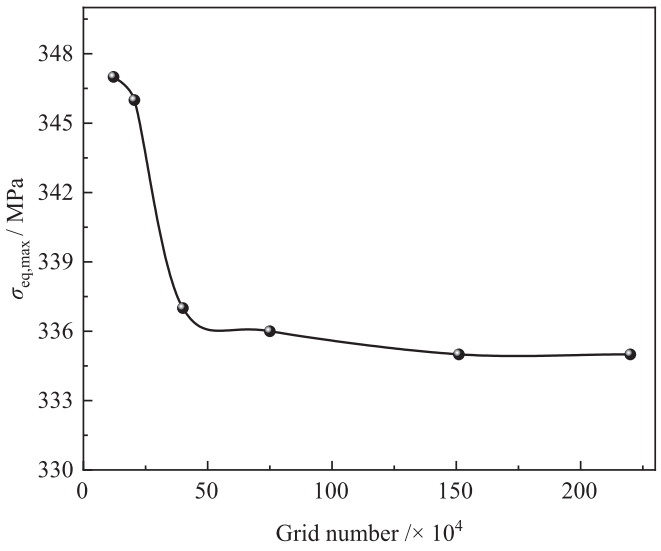


Fig. 5. Grid-independent analysis. The maximum equivalent stress of the tube produced by mass flux $G = 1800$ kg/(m^2·s), heat flux density $q = 240$ kW/m^2, outlet pressure $P = 30$ MPa, and inlet temperature T_{in}=773.15 K.

Table 2
Typical experimental cases for validation

	G,kg/(m^2·s)	L, m	T_{in}, K	P, MPa	d, mm	D, mm	q_w, kW/m^2	Material
Case A	1000	2	393.15	20.6	10	14	200	1Cr18Ni9Ti
Case B	1000	1	673.15	15	30	45	/	Inconel 625
Case C	/	2	753.15	20	16	12	400	Haynes 230

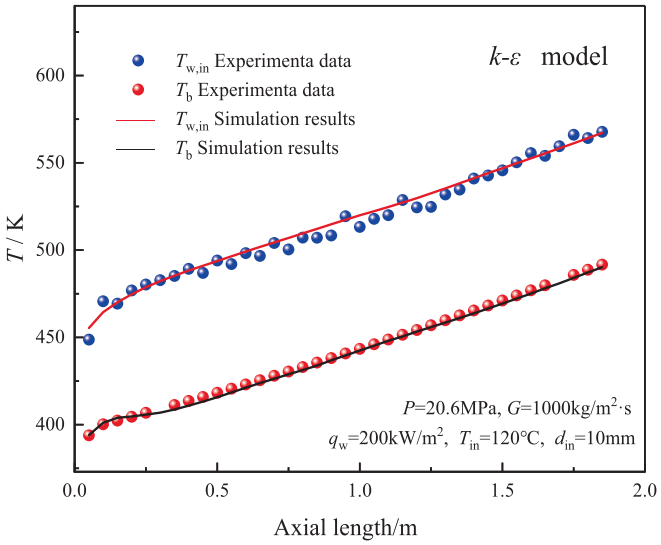


Fig. 6. Comparison between numerical results and experimental data

$$\varepsilon_E^{eq} = \sqrt{\frac{1}{2}\left[\left(\varepsilon_E^1 - \varepsilon_E^2\right)^2 + \left(\varepsilon_E^2 - \varepsilon_E^3\right)^2 + \left(\varepsilon_E^3 - \varepsilon_E^1\right)^2\right]} \tag{20}$$

Where α, E, and ν represent the thermal expansion coefficient, elastic modulus, and Poisson's ratio of Inconel 625 alloy, respectively; ΔT_r is the radial temperature difference of the tube wall, which is calculated as the inner wall temperature T_i minus the outer wall temperature T_o; r_i is the inner radius; r_o is the outer radius.

The boundary conditions are as follows: the inlet temperature is T_{in}; the inner wall surface adopts a logarithmic wall function, while the outer wall is subjected to NUH. To avoid entrance effects, the inlet velocity is assumed to be fully developed. The inner tube wall satisfies a no–slip boundary condition, and the outlet pressure is defined as P. The outlet wall is fixed. The inlet wall is assigned a prescribed displacement and is free to expand in the axial direction, while the remaining walls are also unconstrained. The detailed boundary conditions are shown in Fig. 3.

2.3. Fatigue-creep damage evaluation

2.3.1. Fatigue damage

The total fatigue damage is estimated by Eq. (21). It is defined as the sum of ratios of the N_j cycles and $N_{a,j}$ allowable cycles evaluated for each equivalent strain range $\Delta\varepsilon_{eq,j}$.

$$D_f = \sum_{j=1}^{M} \frac{N_j}{N_{aj}} \tag{21}$$

In this paper, the fatigue damage parameter D_f denotes the damage incurred per transient load cycle.

Typically, the number of allowable cycles is calculated once the strain range is known using an implicit Manson-Coffin expression:

$$\Delta\varepsilon_{eq} = 2\left[\frac{\sigma_f'}{E}(N_f)^{-c_1} + \varepsilon_f'(N_f)^{-c_2}\right] \tag{22}$$

where E' is the dynamic elastic modulus, $\sigma_{f'}$ is fatigue strength coefficient, $\varepsilon_{f'}$ is the fatigue ductility, c_1 and c_2 are constants. These values are shown in Table 1.

The fatigue damage is estimated after the number of allowable cycles, which varies with the strain range. Thus, the equivalent elastic-plastic strain range is calculated as follows:

For $\sigma_{eq}^E \leqslant S_y$, elastic regime, $\Delta\varepsilon_{eq} = \Delta\varepsilon_{eq}^E$

For $\sigma_{eq}^E \geqslant 2S_y$, the equivalent elastic-plastic stress range is obtained following the Neuber method.

$$\Delta\varepsilon_{eq}^E \Delta\varepsilon_{eq}^E = \frac{\Delta\varepsilon_{eq}^2}{E} + 2\Delta\varepsilon\left(\frac{\Delta\varepsilon_{eq}}{2K'}\right)^{\frac{1}{n'}} \tag{23}$$

After that, the equivalent plastic strain range is calculated as [23]

$$\Delta\varepsilon_{eq}^p = 2\left(\frac{\Delta\varepsilon_{eq}}{2K'}\right)^{\frac{1}{n'}} \tag{24}$$

and then the equivalent elastic-plastic strain range is obtained as [24]

$$\Delta\varepsilon_{eq} = \frac{\Delta\sigma_{eq}}{E} + \Delta\varepsilon_{eq}^p \tag{25}$$

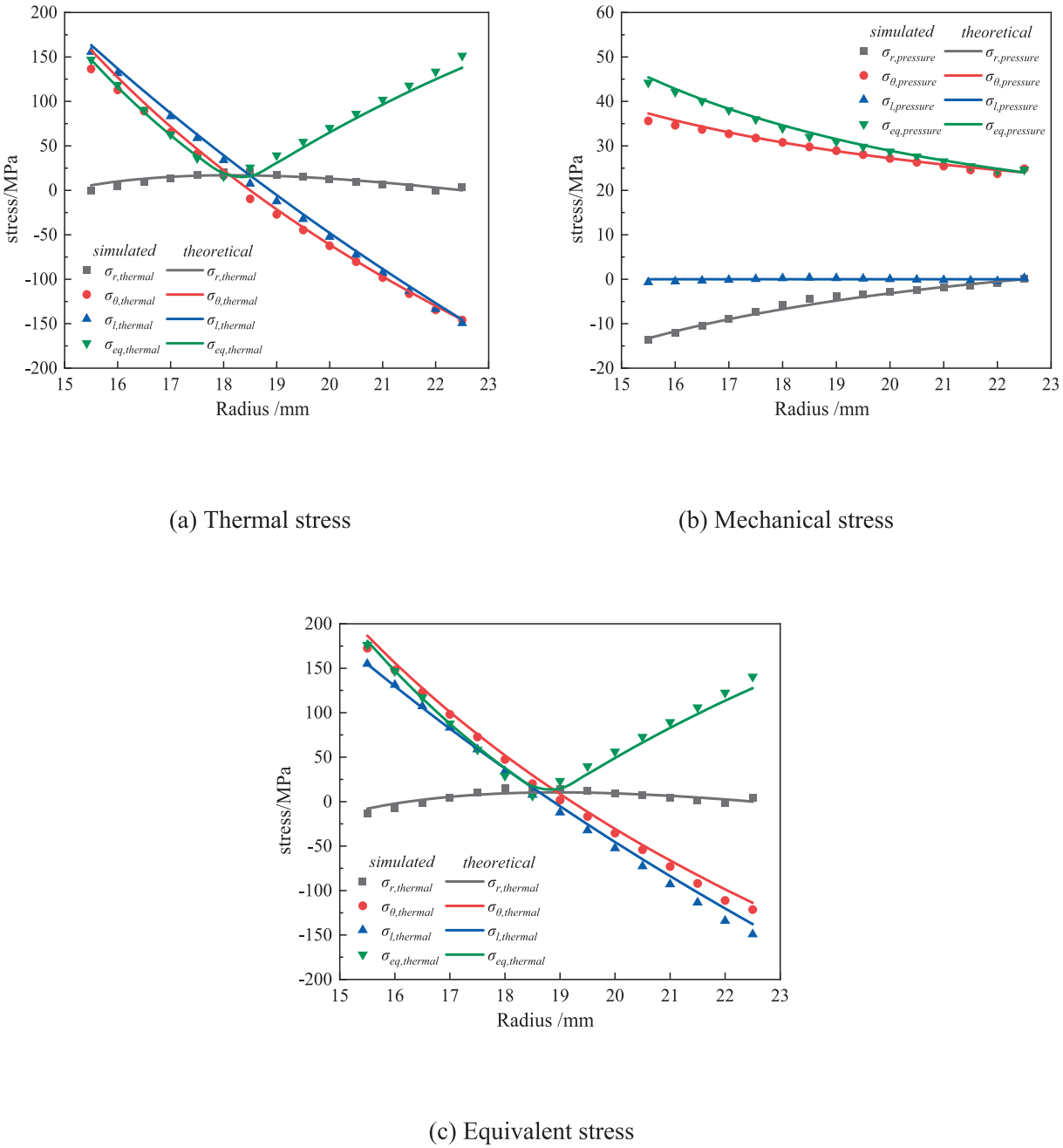
2.3.2. Creep damage

The linear damage summation rule, akin to that used for fatigue damage assessment, represents a prevalent approach for quantifying creep damage accumulation in materials under complex cyclic loading at varying temperatures [25]. Thus, the creep damage is obtained through Eq. (26).

$$D_c = \sum_{i=1}^{N} \frac{dt}{t_R(\sigma_{creep}, T)} \tag{26}$$

where dt is the time step size and t_R is the creep time-to-rupture obtained by the Mendelson-Roberts-Manson (M-R-M) [26] parametrization Eq. (27):

$$\log_{10}(t_R) = \beta_0 + \beta_1\frac{1}{T} + \beta_2\log_{10}(\sigma_{creep}) + \beta_3\log_{10}(\sigma_{creep})\frac{1}{T} \tag{27}$$



(a) Thermal stress

(b) Mechanical stress

(c) Equivalent stress

Fig. 7. Validation of structural model against theoretical results.

where T and σ_{creep} are the temperature and the effective stress experienced by each portion of the cooling wall tubes in each time step.

The effective creep stress to evaluate the time to rupture due to creep damage can be calculated from Eq. (28).

$$\sigma_{\mathrm{creep}} = \sigma_{\mathrm{eq}} - \sigma_{\mathrm{relax}} \tag{28}$$

σ_{relax} refers to stress relaxation [27], and its expression is given by Eq. (29).

$$\sigma_{\mathrm{relax}} = \sigma_{\mathrm{eq}} - E\left[\left(\sigma_{\mathrm{eq}}/E\right)^{1-n} - (1-n)AE^{n}\exp(-Q/RT)\right]^{\frac{1}{1-n}} \tag{29}$$

The fatigue-creep coefficients for Inconel 625 are listed in Table 1.

2.4. Variable Load Regulation Strategy

Currently, S-CO_2 power generation technology has not yet reached maturity for large-scale commercial application. Methods for variable load regulation in S-CO_2 power generation are adapted from operational experience with supercritical water-steam Rankine cycle units in coal-fired power plants [28]. Based on power plant operational data, during peak-shaving processes, the heat flux density (q) and the working fluid mass flux (G) exhibit nearly linear changes [29]. Therefore, a coordinated variation between the cooling wall q and G is employed to achieve variable-load operation in S-CO_2 power generation systems [30]. For example, during the load-increasing process, q increases while G is raised correspondingly. To simplify the analysis, this study assumes that q and G vary in direct proportion to the power plant load as follows. This simplification neglects response delays caused by flame deflection within the furnace and thermal inertia effects at extremely low loads.

Heat flux density (q):

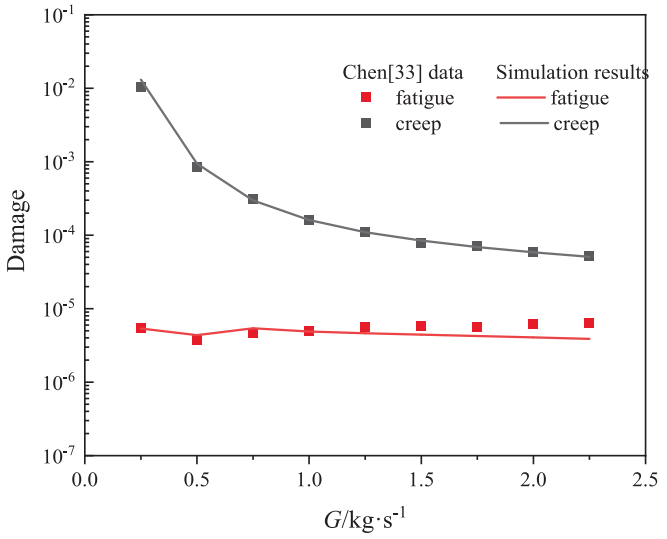


Fig. 8. Validation of fatigue and creep damage model

$$q(t) = q_0 \pm \frac{k}{60} \cdot t \cdot q_1 \tag{30}$$

mass flux (G):

$$G(t) = G_0 \pm \frac{k}{60} \cdot t \cdot G_1 \tag{31}$$

q_0 and G_0 are the initial heat flux density and working fluid mass flow rate, q_1 and G_1 are the heat flux density and mass flow rate at full load. k is the load change rate (%/min) and t is the time (s). The "+" sign corresponds to a load-increasing process, while the "−" sign corresponds to a load-decreasing process. For example, the load-decreasing process is used to illustrate the variations of main parameters, as shown in Fig. 4. During a load reduction from 100% to 25%, G decreases from 1800 kg/(m^2·s) to 450 kg/(m^2·s), while q declines from 240 kW/m^2 to 60 kW/m^2. Five load change rates, ranging from 2% to 6% per minute, were considered.

2.5. Grid independence study

A mesh independence analysis was conducted using the maximum equivalent stress $\sigma_{eq,max}$ on the pipe wall at the mid-section as the convergence criterion. As shown in Fig.5, the calculation results for grids of 0.4 million and above are almost consistent. Considering the convenience in the calculation process, the mesh set was selected in this study.

3. Model validations

Given the extreme scarcity of experimental data on S-CO_2 cooling walls under combined high-temperature, high-pressure, and NUH conditions, this study adopts a tiered validation strategy. The thermal-fluid model is validated against published classical experimental data; the structural model is validated theoretically; and the damage model is validated using published numerical results.

The S-CO_2 turbulence experimental data under high temperatures, pressures, and heat fluxes are limited. Consequently, the experimental results of Zhu et al. [31] were selected to validate the thermodynamic model. Detailed experimental conditions are shown in Table 2 (Case A). As shown in Fig. 6, the simulated average fluid temperature agrees well with the experimental data, exhibiting a maximum relative error of 0.81%. The relative error of the inner tube wall temperature is 1.25%, confirming the accuracy of the thermodynamic model.

As it was challenging to measure the stress in the cooling wall tube with the high heat flux, the mechanical model was verified using a theoretical method. The radial temperature and pressure difference between the inner and outer wall were 90 K and 20 MPa, respectively. The detailed operating conditions are listed in Table 2 (Case B). As illustrated in Fig. 7, the theoretical predictions for thermal and mechanical stresses are in excellent agreement with the numerical results, exhibiting an average error below 7.5%. This agreement confirms the validity of the proposed multi-physics model.

Direct experimental measurement of fatigue and creep damage on the cooling wall poses significant challenges. For validation of the proposed thermal, structural, and fatigue-creep models, our numerical results were compared with those reported by Chen [14]. The detailed operating conditions are listed in Table 2 (Case C). In this validation case, S-CO_2 was adopted as the heat transfer fluid, with mass flow rates varying from 0.25 to 2 kg/s. As depicted in Fig. 8, the relative errors for fatigue damage and creep damage are 21% and 6%, respectively. These values lie substantially below the 30% acceptance criterion typically stipulated for life-damage assessment [32], thereby affirming the credibility of the present model.

4. Results and discussions

4.1. Characteristics of temperature, stress and fatigue-creep damage

A typical 100% load condition was selected to investigate the temperature and stress distribution of the cooling wall, with the following parameters: mass flux G = 1800 kg/(m^2·s), heat flux density q = 240 kW/m^2, outlet pressure P = 30 MPa, and inlet temperature T_{in}=773.15 K.

Fig. 9 presents the temperature distribution in the cooling wall under various load conditions. The circumferential temperature profile mirrors

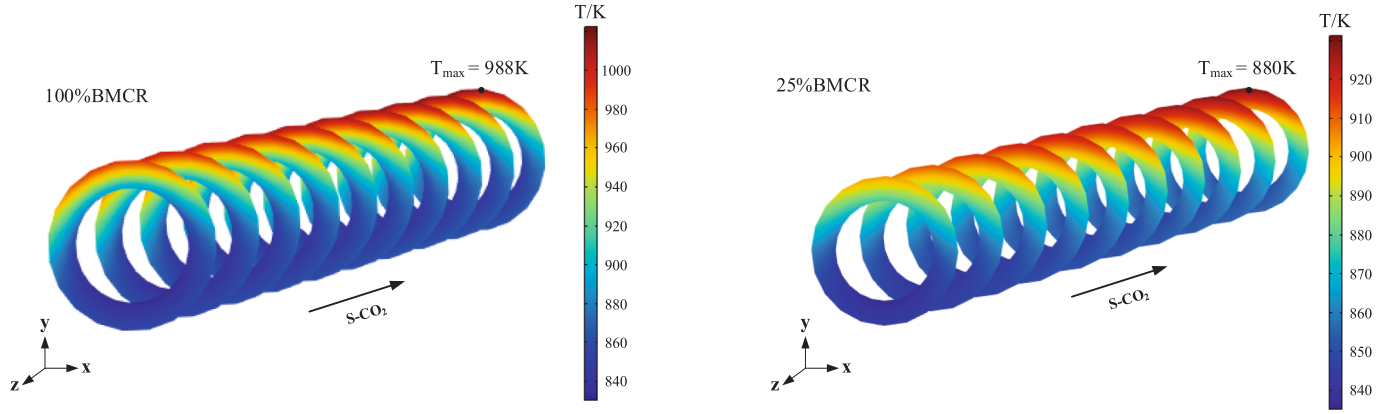


Fig. 9. Temperature profiles of the cooling wall tube at 100% and 25% load conditions.

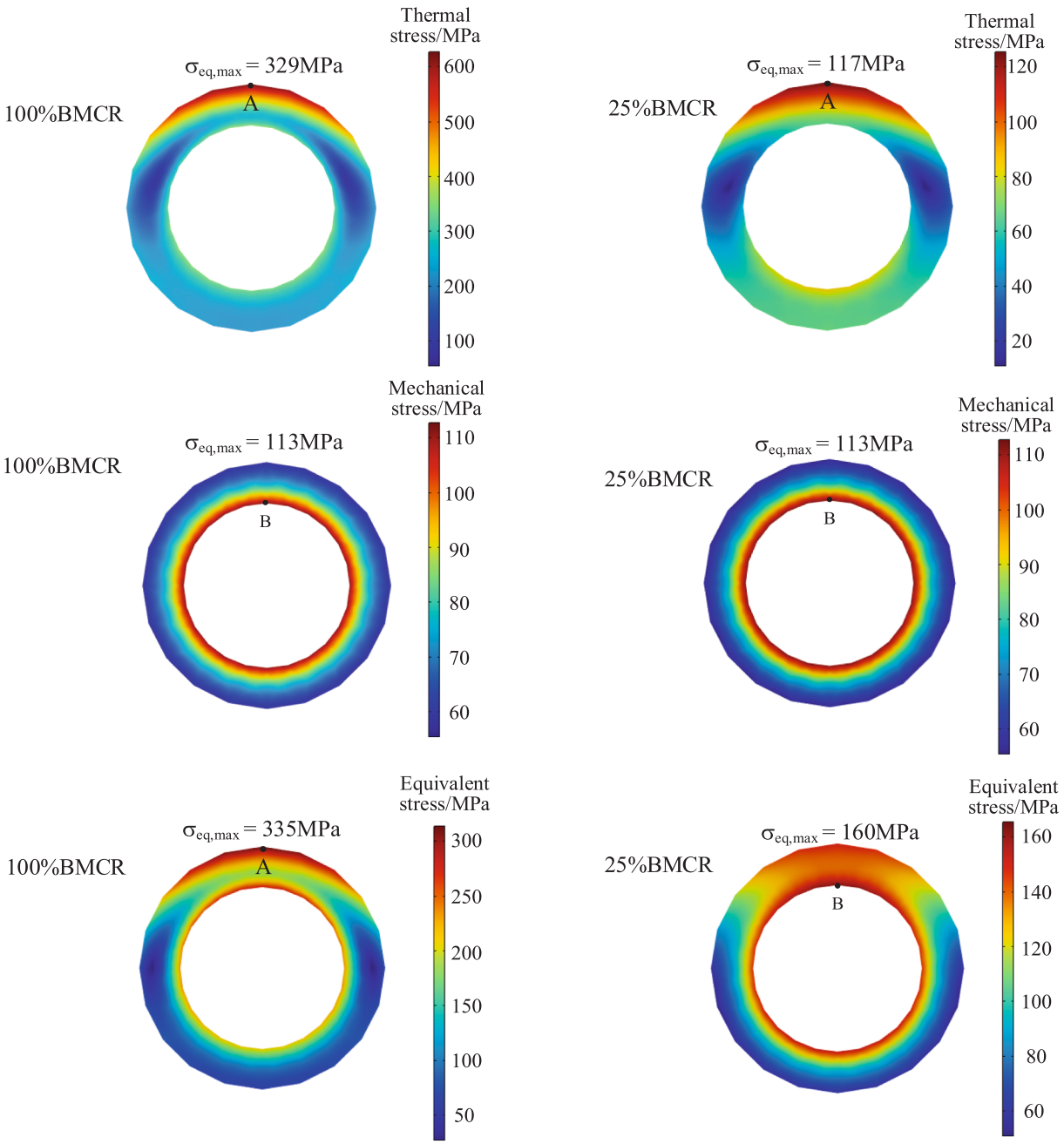


Fig. 10. Profiles of von Mises equivalent stress in the cooling wall tube at 100% and 25% load conditions(z=0.5m).

the applied NUH. The maximum temperature across the tube wall occurs at the 180° position on the fire-facing side. As the load decreases from 100% to 25%, the tube peak temperature drops from 998 K to 880 K, a reduction of approximately 118 K.

Fig. 10 shows that under 100% load, the maximum sectional thermal stress of 329 MPa occurs at point A on the outer wall, while the maximum sectional mechanical stress of 113 MPa is located at point B on the inner wall. At 25% load, the maximum sectional thermal stress at point A decreases to 117 MPa, representing a 64.4% reduction. The mechanical stress remains constant because the pressure differential across the tube wall does not change. Under 100% load, the maximum von Mises equivalent stress (335 MPa) occurs at point A on the outer wall. When the load is reduced to 25%, the location of the maximum equivalent stress shifts from point A on the outer wall to point B on the inner wall. The stress value at this point is 160 MPa, corresponding to a 52.2% decrease.

At 100% load, thermal stress significantly exceeds mechanical stress and therefore dominates the total wall stress. At 25% load, however, thermal and mechanical stresses become comparable in magnitude. The location of the maximum equivalent stress within the cooling wall cross-section is load-dependent: it is situated on the outer wall under high load and transitions to the inner wall under low load. During peak-shaving operations, load fluctuations impose significant combined thermal-mechanical shock on the tube wall structure.

To study the cooling wall's damage characteristics, the system load was increased from 25% to 100% at a rate of 2%/min with G and q varying at the same rate, and the total ramp-up duration was 2250 seconds. Four critical points (A, B, C, D) were selected on the cooling wall at axial positions $z = 0.5$ m and $z = 1.0$ m, as shown in Figs. 11 and 12. These points correspond to the locations of peak temperature and maximum stress within their respective cross-sections. The transient evolution of temperature and stress at these points during the load-

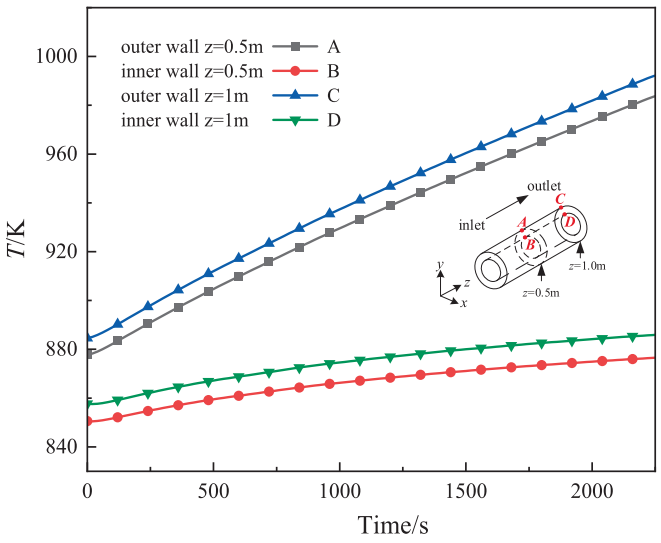


Fig. 11. Evolution of temperature distributions in the cooling wall tube during the transient load increase.

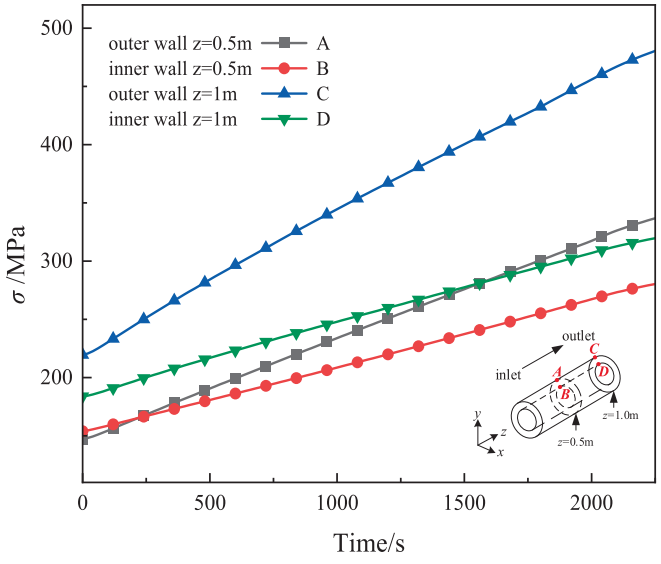


Fig. 12. Evolution of stress distributions in the cooling wall tube during the transient load increase.

increasing process was analyzed.

The temperatures at points A, B, C, and D rise from their initial values of 877.7 K, 850.6 K, 884.6 K, and 857.7 K to 983.7 K, 876.5 K, 991.2 K, and 885.9 K at the end of the process, respectively (as shown in Figs. 11). Notably, the peak temperature (991.2 K) is located at point C on the outer wall of the outlet cross-section ($z = 1.0$ m). This point also exhibits the most pronounced temperature rise of 106.6 K during the load increase.

The equivalent stresses at points A, B, C, and D increase from initial values of 147.2 MPa, 153.7 MPa, 219.5 MPa, and 183.8 MPa to 336.5 MPa, 280.4 MPa, 480.6 MPa, and 319.6 MPa, respectively (as shown in Fig. 12). The maximum stress of the cooling wall locates at the outer wall of the outlet cross-section (point C), which also undergoes the largest stress change during the transient process, with an increase of 261.1 MPa.

Fig. 13 shows damage characteristics at points A, B, C, and D during a single load-increase transient. The initial fatigue damage values at points A, B, C, and D are 1.03×10^{-11}, 2.51×10^{-10}, 3.09×10^{-10} and 6.51×10^{-10}, respectively. These values rise to 1.24×10^{-8}, 2.21×10^{-8}, 5.67×10^{-7} and 5.79×10^{-8} at 100% load. The maximum fatigue damage occurs at point C, which also exhibits the largest increase in fatigue damage (5.66×10^{-7}) during the transient load increase. The initial creep damage values at points A, B, C, and D are 5.99×10^{-12}, 8.56×10^{-11}, 2.65×10^{-10} and 2.96×10^{-10}, respectively. The creep damage increases to 5.76×10^{-8}, 2.15×10^{-8}, 1.33×10^{-6} and 6.62×10^{-8} at 100% load. Similarly, the maximum creep damage occurs at point C. This point also experiences the most significant increase in creep damage (1.33×10^{-6}) during the transient process.

Both fatigue and creep damage increase with the wall temperature, which itself rises with increasing load. Creep damage exhibits a stronger temperature dependence than fatigue damage.

Under low-load conditions, creep damage at all monitored points is lower than fatigue damage, making fatigue damage dominant. As the load (and consequently the wall temperature) increases, creep damage exceeds fatigue damage and becomes the dominant damage mechanism at points A, C, and D.

4.2. Dynamic Characteristics of Cooling Wall Tubes

4.2.1. Effect of load change rate

Five representative load change rate working conditions (Table 3) were selected to investigate the influence of the load change rate on the maximum temperature, stress, fatigue and creep damage in the cooling wall tube.

Figs. 14 and 15 illustrate the influence of the load change rate on the maximum radial temperature difference ($\Delta T_{r,max} = |T_{i,max} - T_{o,max}|$, where $T_{i,max}$ is the maximum inner wall temperature, and $T_{o,max}$ is the maximum outer wall temperature) and von Mises stress distribution at $z = 0.5$ m.

Three operational phases are considered: load decrease (100% to 25%), steady state at 25% load, and load increase (25% to 100%).

Fig. 14 shows that the trends observed during the load decrease and load-increasing processes are symmetrical. This symmetry originates from the idealized assumption that mass flux and heat load vary proportionally. This assumption neglects practical complexities such as flame deflection and non-uniform flow distribution under ultra-low load conditions. In both the load decrease and increase processes, a higher load change rate induces a greater rate of change in $\Delta T_{r,max}$, signifying more severe thermal shock. During rapid load transients, abrupt variations in q induce an almost instantaneous response of the $T_{o,max}$, whereas the inner wall exhibits a pronounced thermal lag due to tube thermal inertia. This temporal disparity between the inner- and outer-wall thermal responses consequently intensifies the radial temperature gradient. As the load change rate increases from 2%/min to 6%/min, the rate of change in $\Delta T_{r,max}$ rises from 0.052 K/s to 0.161 K/s — an increase of approximately 3.1 times.

Fig. 15 presents the evolution of the von Mises equivalent stress at A and B. As the load ramp rate increases, the time derivative of the equivalent stress rises correspondingly, indicating intensified thermo-mechanical stress transients. The peak stress rate occurs near the midpoint of the transient loading interval. When the load ramp rate is increased from 2%/min to 6%/min, the equivalent stress rate at Point A rises from 0.156 MPa/s to 0.461 MPa/s—an increase of approximately 2.95 times. Similarly, at Point B, the stress rate increases from 0.101 MPa/s to 0.261 MPa/s, representing an increase of about 2.62 times.

Point A, located on the outer wall at the fire-exposed side, exhibits an equivalent stress predominantly governed by thermal stress. By contrast, Point B, situated on the inner wall, experiences equivalent stress comprising both constant mechanical stress and transient thermal stress, where the mechanical component is independent of the load change rate. Under high-load conditions (100% load), the equivalent stress at Point B is still dominated by thermal stress; whereas under low-load conditions (25)% load), mechanical stress becomes prevailing as thermal stress diminishes. Furthermore, the temperature at Point A responds

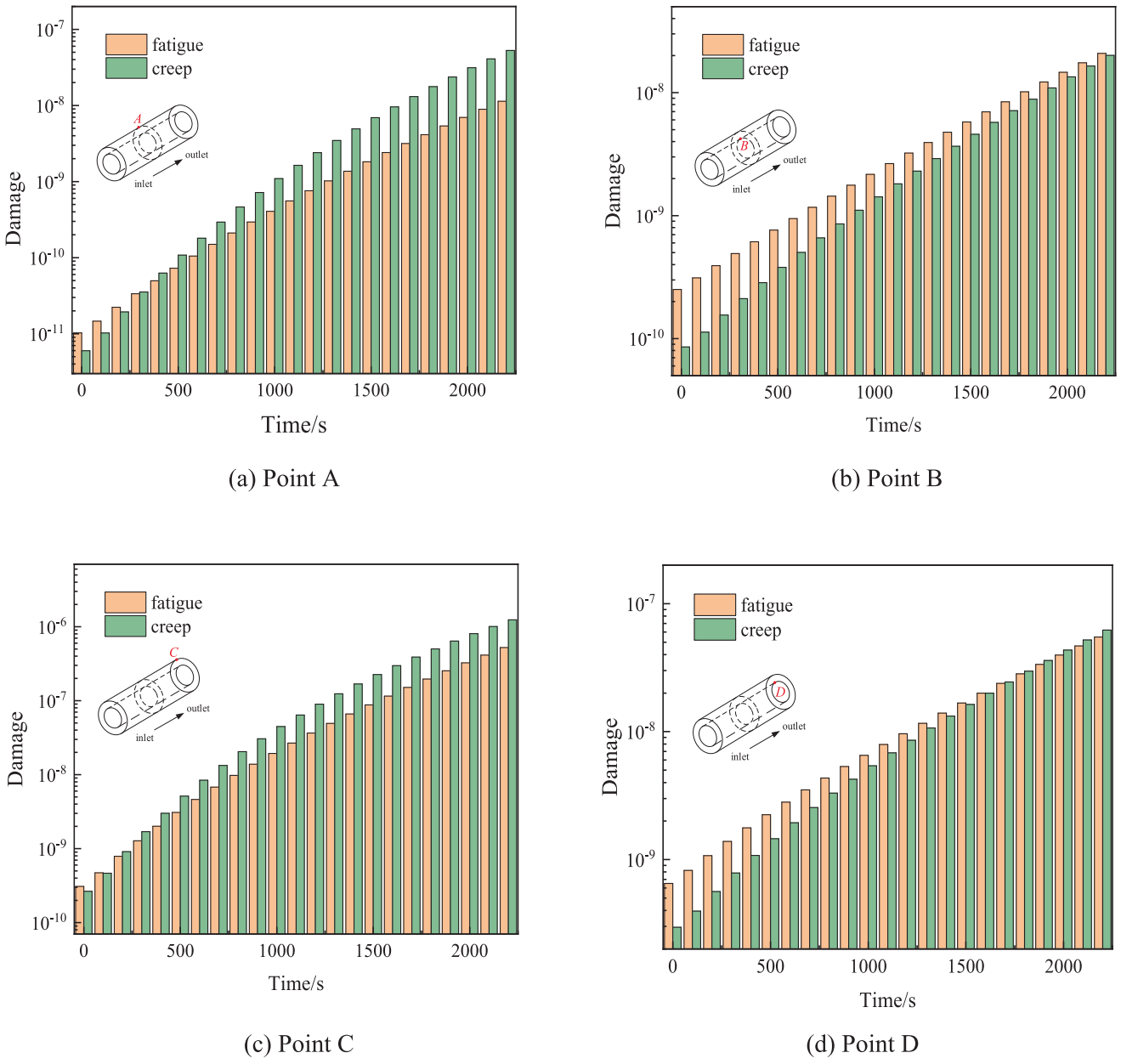


Fig. 13. Evolution of damage at points A, B, C, and D in the cooling wall during the transient load cycle.

Table 3
Load change rate working conditions.

Case	Load Change Rate/%·min^{-1}	Duration (t/s)
a	2	2250
b	3	1500
c	4	1125
d	5	900
e	6	750

instantaneously to q, whereas at Point B, it is also modulated by convective heat transfer with the internal S–CO_2 flow, leading to a slower rate of thermal stress variation at Point B compared with Point A. Collectively, these two factors render the equivalent stress at Point B substantially less sensitive to the load change rate than that at Point A. This quantitatively elucidates the underlying mechanism for the greater sensitivity of the thermal–stress–dominated outer–wall region to load change rate.

Figs. 16 and 17 show that damage in the cooling wall tube increases with load change rate. A higher load change rate leads to a more rapid wall temperature change, thereby accelerating the accumulation of both fatigue and creep damage. At a load change rate of 2%/min, the increase in damage is minimal. Specifically, at t = 800 s, the fatigue damage reaches 8.80×10^{-8}, and the creep damage reaches 2.02×10^{-7}. In contrast, when the load change rate increases to 6%/min, damage accumulates rapidly, with fatigue and creep damages reaching 2.85×10^{-6} and 4.72×10^{-6}, respectively, at the same time point. Consequently, as the load change rate rises from 2%/min to 6%/min, creep damage increased by 31.3 times and fatigue damage increased by 22.4 times. These results demonstrate that the load change rate significantly influences tube wall damage. This can be attributed to the fact that a higher load change rate induces a substantial temperature gradient across the tube wall over a short period. This gradient, in turn, generates high-amplitude cyclic thermal stresses, which accelerate low-cycle fatigue damage. Concurrently, transient temperature peaks and sustained thermal stresses act synergistically to promote creep damage

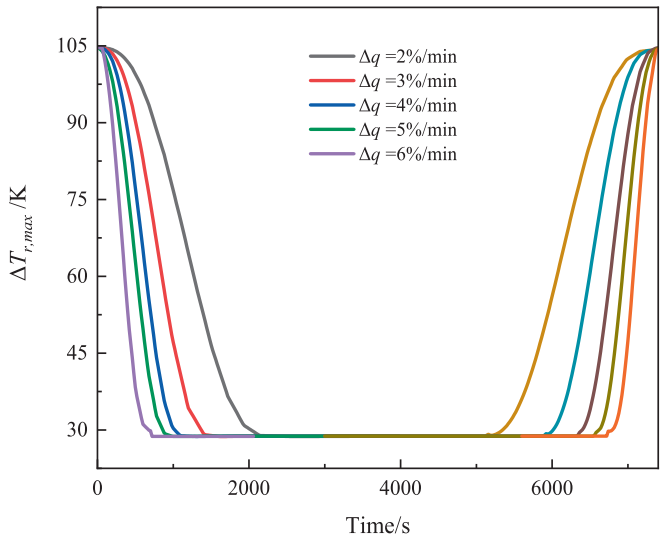


Fig. 14. $\Delta T_{r,max}$ evolution at z = 0.5 m during load-increasing and load-decreasing process.

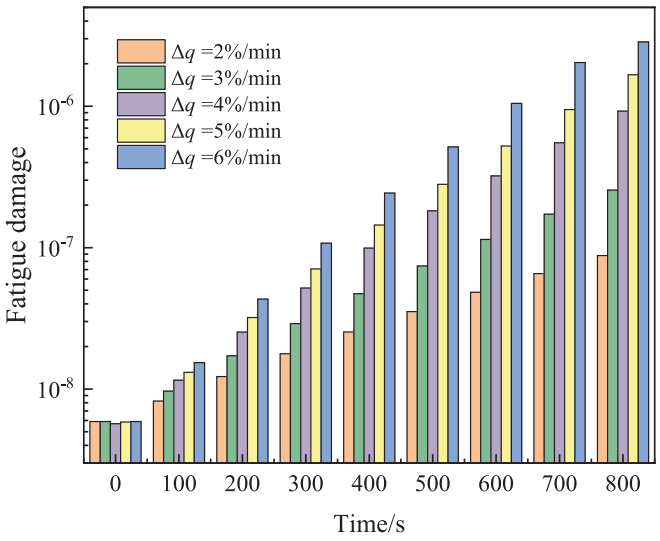


Fig. 16. Influence of the load change rate on the fatigue damage in the cooling wall.

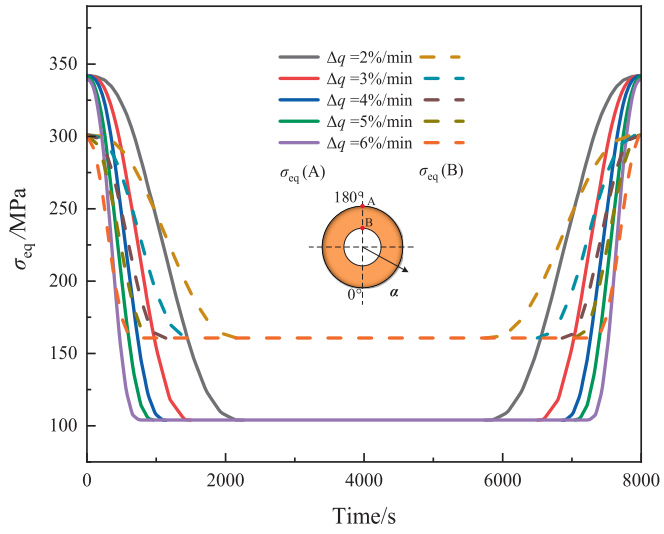


Fig. 15. von Mises equivalent stress evolution at A and B (z = 0.5 m) during load-increasing and load-decreasing process.

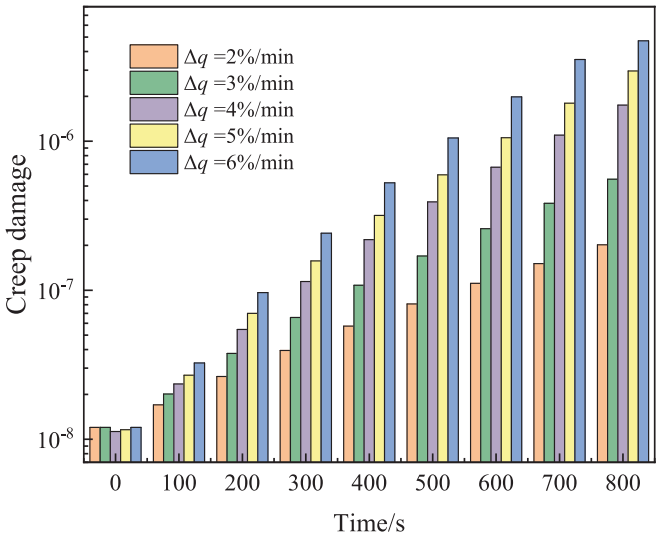


Fig. 17. Influence of the load change rate on the creep damage in the cooling wall.

accumulation. Furthermore, fatigue and creep do not operate as independent damage mechanisms; rather, their synergistic interaction further accelerates the overall damage progression.

4.2.2. Sensitivity Analysis

The influence of key operational parameters on cooling wall tube was analyzed under the typical 100% load condition. The ratio of the calculation results after changing an operating parameter to those under typical operating conditions is denoted as *.

The maximum sectional thermal stress is positively correlated with the circumferential temperature difference (ΔT) [33]. Therefore, controlling ΔT is critical to prevent the wall stress from exceeding the material's yield strength and avoiding tube failure.

First, key operational parameters — including operating pressure (P), mass flux (G), inlet temperature (T_{in}), and heat flux (q) —were identified. Then, using the principle of varying a single variable while keeping the other parameters constant, the corresponding dimensionless ratio ΔT^* was calculated as follows:

$$\Delta T^* = \frac{\Delta T_i}{\Delta T_{ref}} \tag{32}$$

where the subscripts "*ref*" and "*i*" denote the typical 100% load condition and the corrected parameter condition, respectively.

The parameters are ranked in descending order of influence on ΔT as follows: $q > T_{in} > G > P$, with q exerting the greatest influence and P the least (as shown in Fig. 18). When each parameter decreases from 1.0 to 0.4, ΔT^* for q drops to 0.438, indicating a positive correlation. ΔT^* for G and T_{in} rises to 1.42 and 1.533, respectively, indicating negative correlations, while ΔT^* for P remains essentially unchanged (as shown in Fig. 19).

4.2.3. Load increase and decrease process

The aforementioned sensitivity analysis indicates that the ΔT exhibits a positive correlation with the heat flux density (q) and a negative correlation with the mass flux (G). To reduce the ΔT, peak temperature, and stress in the cooling wall, a load–control strategy was adopted. The rationale behind this strategy lies in the active compensation of the

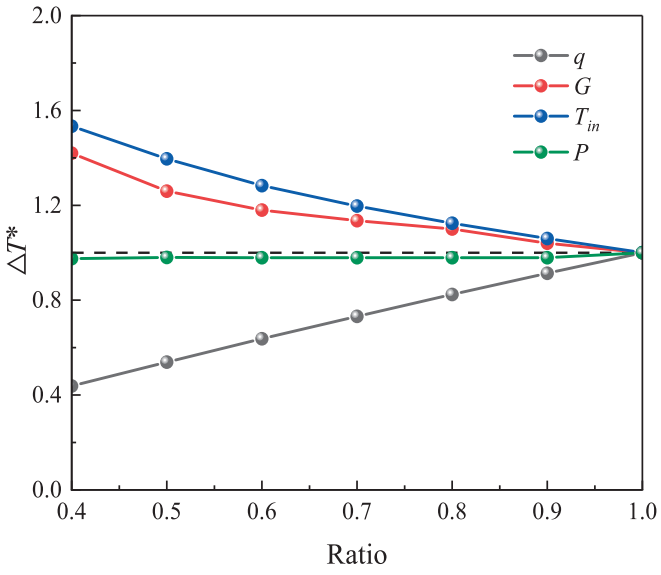


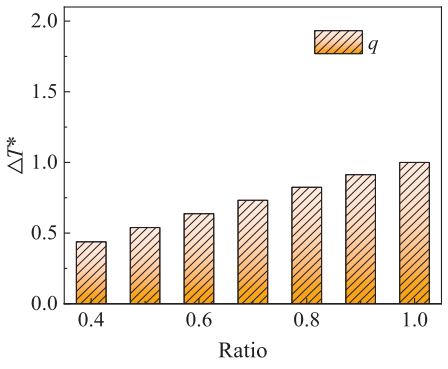
Fig. 18. △T^* as a function of key parameters

dynamic mismatch in thermal inertia between the furnace and the cooling wall, as elaborated in the following.

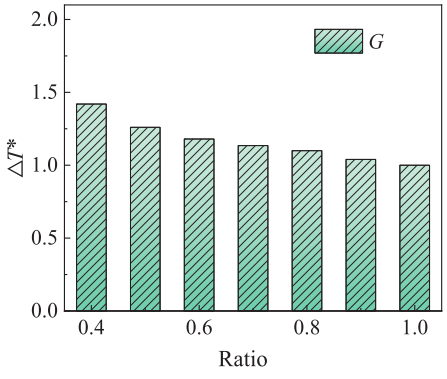
During the load-decreasing process, the change rate of heat flux (Δq) was increased, as shown in Fig. 20**(a)**. At the onset of the transient, Δq rose rapidly and then returned to zero once the steady state was reestablished. Notably, the average value of Δq over the entire transient period was maintained equal to that of the coolant mass flux change rate (ΔG). When q and G decreased synchronously, the residual heat stored in the furnace kept diffusing inward through the tube walls, whereas the internal convection had already weakened. This asynchrony resulted in a temperature overshoot on the wall. Hence, elevating Δq contributed to diminishing the radial temperature gradient, thereby easing the thermal shock during the transient.

During the load–increasing process, ΔG was raised, as shown in Fig. 20**(b)**. Similarly, ΔG increased rapidly at the transient onset and then returned to zero upon stabilization, with its average change rate over the entire process maintained equal to that of Δq. If q and G were increased simultaneously, the rapid rise in heat input at the outer wall—compounded by the delayed convective cooling response due to flow development and radial heat diffusion through the tube wall—would cause a sharp increase in wall temperature. Under such circumstances, increasing ΔG ahead of time enhances the internal convective heat transfer, thereby accelerating heat removal from the wall to the working fluid.

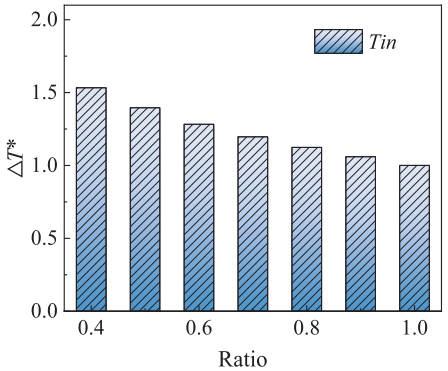
Fig. 21 shows the evolution of the cooling wall temperature, fluid outlet temperature, and stress distribution under conditions where ΔG is held constant at 4%/min, while Δq is progressively increased. Results show that both the peak temperature and the stress at point A decrease as Δq increases. From the perspective of cooling wall safety, a higher Δq during load-decreasing process is beneficial. However, the fluid outlet temperature decreases with an increasing q rate. The fluctuation of the



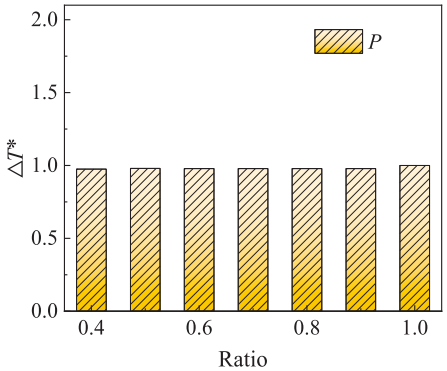
(a) The effect of q on ΔT^*



(b) The effect of G on ΔT^*

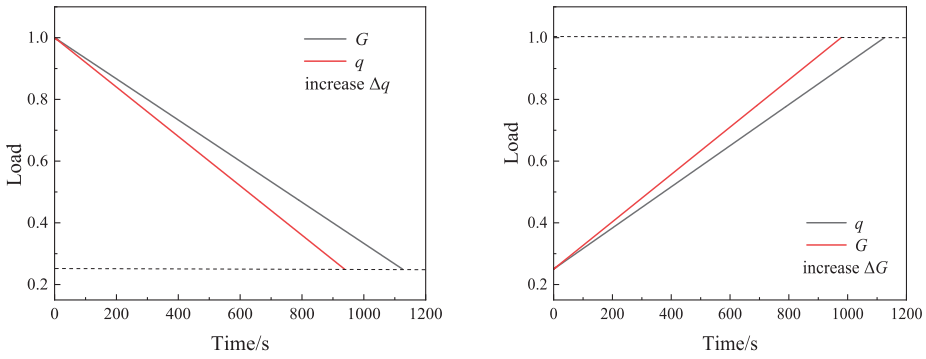


(c) The effect of T_{in} on ΔT^*



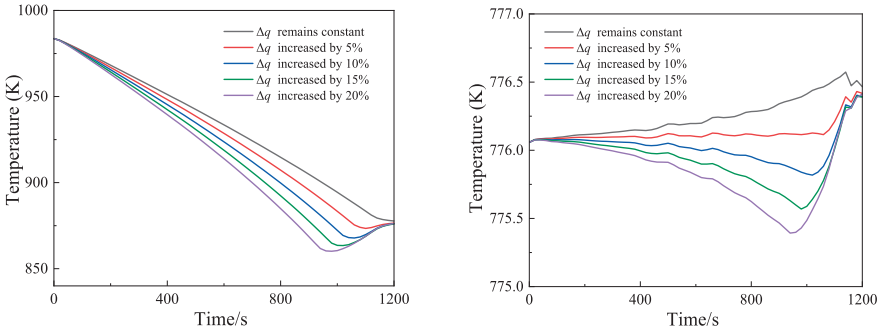
(d) The effect of P on ΔT^*

Fig. 19. Key parameter sensitivity analysis.

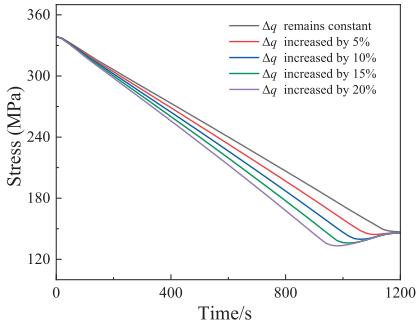


(a) Load-decreasing process (b) Load-increasing process

Fig. 20. Load change rate regulation methods



(a) Temperature variation at point A (z=0.5m) (b) Export Fluid Temperature Response



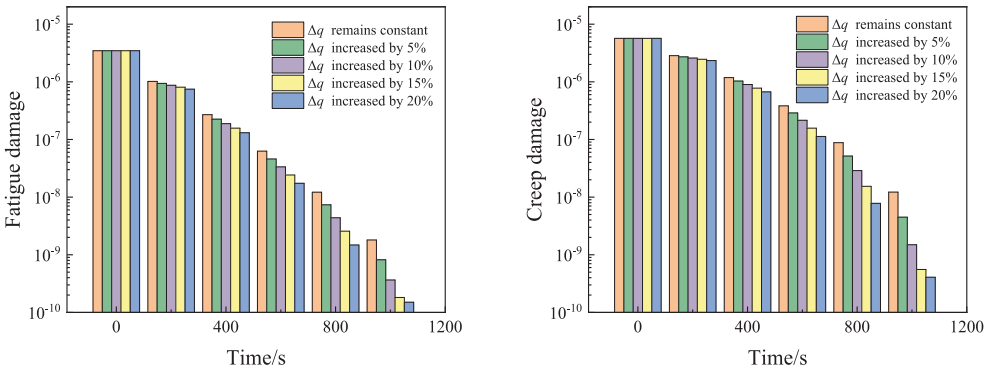
(c) Stress variation at point A (z=0.5m)

Fig. 21. Cooling wall characteristics during load-decreasing process

outlet temperature exhibits a non-monotonic dependence on Δq, decreasing initially and then increasing as Δq rises. Considering overall system stability, an optimal condition is achieved when Δq is increased by approximately 5% relative to the baseline rate. Therefore, for the load-decreasing process with a fixed ΔG of 4%/min, an optimal Δq of 4.2%/min was selected. Compared with both ΔG and Δq set at 4%/min, the optimized protocol reduces the average temperature at point A from 931.94 K to 927.02 K, a decrease of 4.92 K. Meanwhile, the average stress drops from 239.94 MPa to 233.60 MPa, a reduction of 6.34 MPa. In summary, the optimization reduces both average temperature and stress throughout the load reduction process, while concurrently enhancing overall system stability.

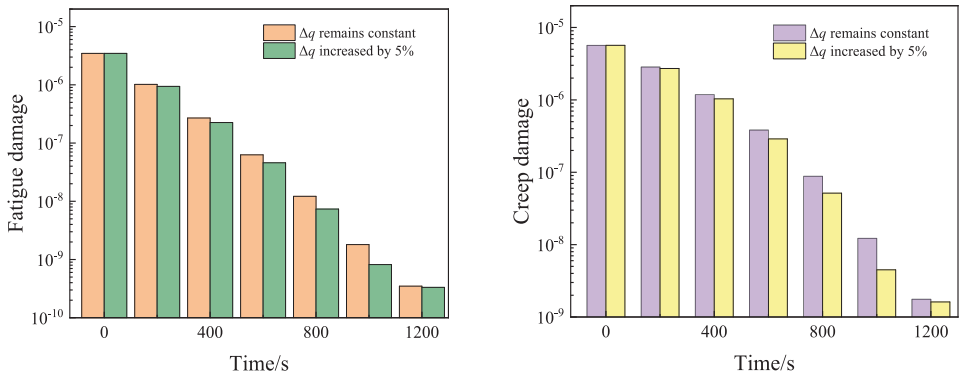
Fig. 22 illustrates fatigue-creep damage in the cooling wall as ΔG is held constant at 4%/min, while Δq is progressively increased. Results show that both fatigue and creep damage at point A decrease as Δq increases. Furthermore, fatigue damage remains lower than creep damage in all cases examined. When Δq is increased from 4%/min to 4.8%/min, the fatigue damage at point A at $t = 1125$ s decreases from 5.14×10^{-10} to 2.69×10^{-10}, corresponding to a reduction of approximately 1.9 times. Meanwhile, the creep damage decreases from 2.79×10^{-9} to 1.09×10^{-9}, representing a reduction of about 2.5 times. Therefore, increasing Δq during the load reduction process contributes to the safe operation of the cooling wall.

Fig. 23 shows the damage comparison at point A ($z = 0.5$ m) during



(a) Fatigue damage at point A (z=0.5m) (b) Creep damage at point A (z=0.5m)

Fig. 22. Damage characteristics of cooling wall during load-decreasing process



(a) Fatigue damage comparison (b) Creep damage comparison

Fig. 23. Damage Comparison of cooling wall during load-decreasing process

the load-decreasing process with ΔG = 4%/min and Δq = 4.2%/min. The fatigue and creep damage in the cooling wall tube at point A reach 3.48×10^{-10} and 1.76×10^{-9} at t = 1200 s, respectively. Compared with both ΔG and Δq set to 4%/min, the corresponding damage values at t = 1200 s are 3.32×10^{-10} (fatigue damage) and 1.61×10^{-9} (creep damage). The optimized strategy reduces fatigue damage by 4.52% and creep damage by 8.36% at point A over the entire load-decreasing process. In addition, it enhances system operational stability.

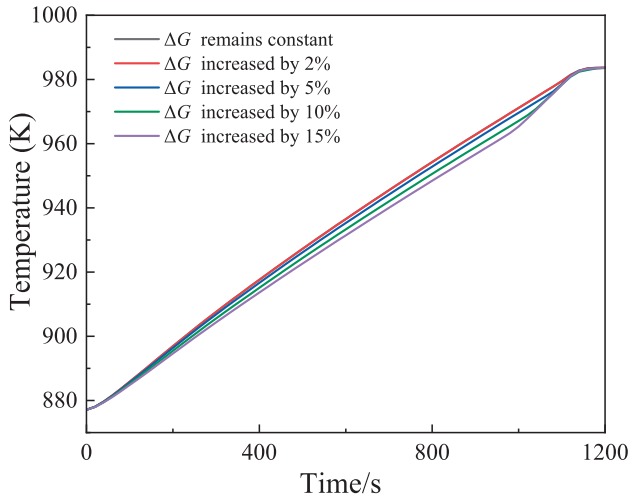
Fig. 24 shows the distributions of cooling wall temperature, fluid outlet temperature, and stress under conditions where Δq is held constant at 4%/min, while ΔG is gradually increased. Results show that both the peak temperature and the stress at point A decrease with increasing ΔG. From the perspective of cooling wall safety, a higher ΔG is favorable during the load-increasing process. However, the fluctuation of the outlet temperature also decreases as ΔG rises. The fluctuation of the outlet temperature exhibits a non-monotonic dependence on ΔG, decreasing initially and then increasing as ΔG rises. Considering overall system stability, an optimal trade-off is achieved when ΔG is increased by approximately 2% relative to the baseline. Therefore, for the load-increasing process with a fixed Δq of 4%/min, an optimal ΔG of 4.08%/min was chosen.

Compared to both Δq and ΔG set at 4%/min, the optimized protocol reduced the average temperature at point A from 935.28 K to 934.59 K, a decrease of 0.69 K. Meanwhile, the average stress was lowered from 247.56 MPa to 246.92 MPa, representing a reduction of 0.64 MPa. In summary, this optimization decreases both the average temperature and average stress during the load-increasing process, while further improving the overall stability of the system.

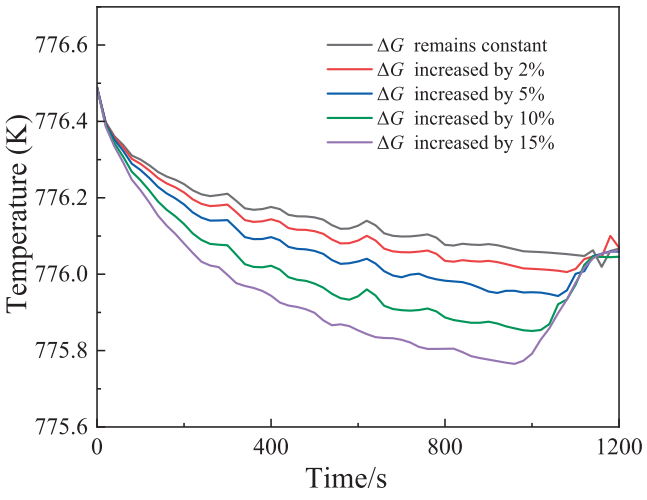
Fig. 25 illustrates fatigue-creep damage in the cooling wall under conditions where Δq is held constant at 4%/min, while ΔG is gradually increased. The results show that both fatigue and creep damage at point A decrease as ΔG increases. When ΔG is increased from 4%/min to 4.6%/min, the fatigue damage at point A at t = 1200 s decreases from 3.25×10^{-6} to 3.02×10^{-6}, corresponding to a reduction of approximately 7.1%. Meanwhile, the creep damage decreases from 5.48×10^{-6} to 5.27×10^{-6}, — a decrease of approximately 3.8%. Therefore, increasing ΔG during the load-increasing process is beneficial for the safe operation of the cooling wall.

Fig. 26 shows the damage comparison at point A during the load-increasing process with Δq of 4%/min and ΔG of 4.08%. The fatigue and creep damage at point A are 3.12×10^{-6} and 5.37×10^{-6}, respectively, at t = 1200 s. In contrast, the corresponding damage values are 3.25×10^{-6} (fatigue damage) and 5.48×10^{-6} (creep damage) under the baseline strategy ($\Delta G = \Delta q$ = 4%/min). Through this optimization, fatigue damage and creep damage in the cooling wall are reduced by 4% and 2%, respectively, over the entire load-increasing process, while simultaneously enhancing system operational stability.

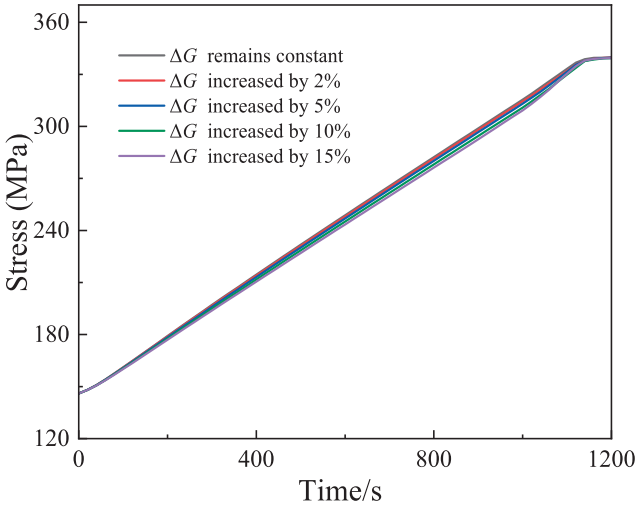
Further quantification of the optimization margins indicates that load reduction requires approximately 5% elevation in Δq, while load increase demands only 2% increase in ΔG. This discrepancy reflects the inherent thermal–inertia imbalance between the two sides. The furnace side, with its significantly greater thermal inertia, is prone to



(a) Temperature variation at point A (z=0.5m)



(b) Export Fluid Temperature Response



(c) Stress variation at point A (z=0.5m)

Fig. 24. Cooling wall characteristics during load-increasing process

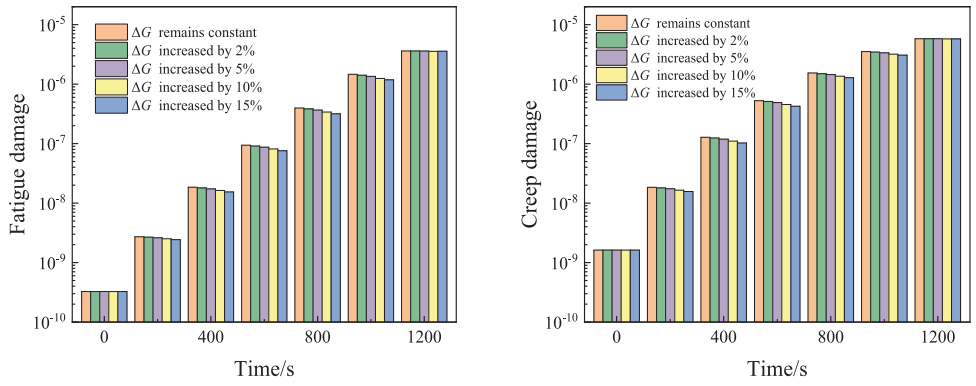
overheating during load reduction, thereby calling for more pronounced modulation of heat input. In the load–increasing regime, however, the lower inertia on the fluid side means that a modest advance in cooling capacity suffices to accommodate the rising heat flux.

4.3. Optimization of load change rate matching

As concluded in Section 4.1, fatigue damage dominates under low-load conditions, whereas creep damage dominates in the high-load region. Adopting a lower load change rate under low-load conditions aims to mitigate fatigue damage. Conversely, employing a higher load change rate during low-load operation induces a greater temperature change rate, which in turn exacerbates fatigue damage.

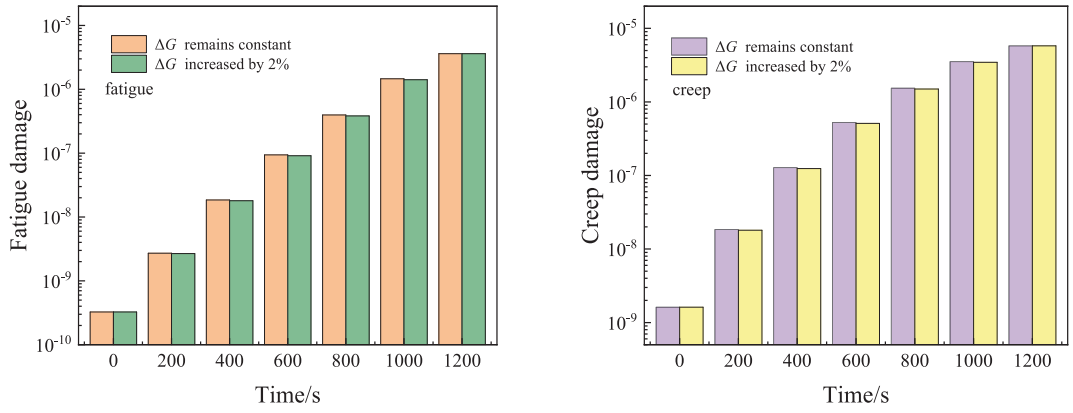
Fig. 27 shows the variation of the maximum wall temperature (T_{max}) with load change rates during the load-increasing process. For all load change rates, T_{max} starts at 883.6 K and, because the initial and final conditions are identical, the system reaches the same final thermal equilibrium of 991.8 K, while the transient temperature rise rate is significantly affected. Increasing the load change rate from 2%/min to 6%/min raises the T_{max} increase rate from 0.048 K/s to 0.144 K/s, an approximately threefold increase.

Optimizing the matching between load change rates and system load entails adopting higher load change rates at high loads and lower rates at low loads. Based on this principle, a quadratic-function-based method for determining the load change rate is proposed, as illustrated in Fig. 28 **(b)**. This method adopts a second-order polynomial fit, with the derivative of the quadratic function (instantaneous load change rate) specified as 2.5%/min at 25% load and 5%/min at 100% load. Accordingly, the load change rate increases progressively during load increase, achieving a favorable match between load change rates and system load



(a) Fatigue damage at point A (z=0.5m) (b) Creep damage at point A(z=0.5m)

Fig. 25. Damage characteristics of cooling wall during load-increasing process



(a) Fatigue damage comparison (b) Creep damage comparison

Fig. 26. Damage Comparison of cooling wall during load-increasing process

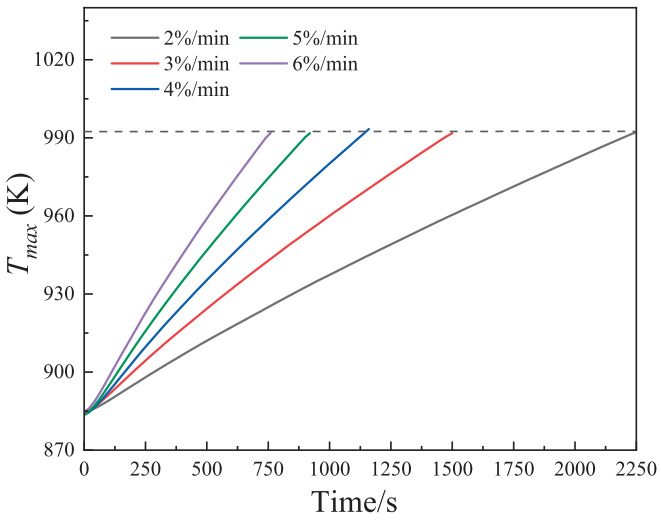


Fig. 27. Effect of load change rate on maximum wall temperature

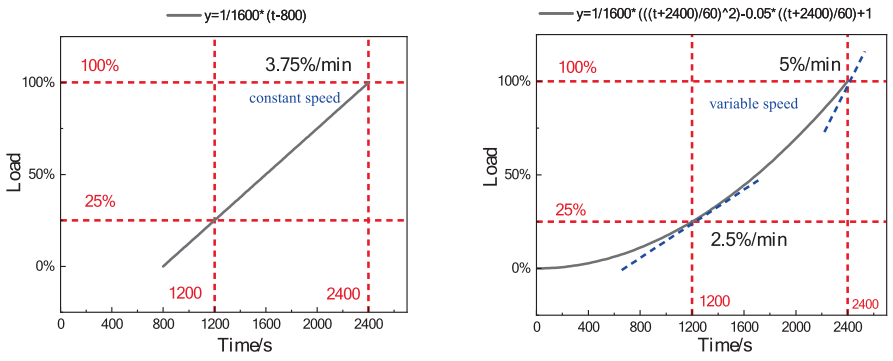
levels.

A comparative investigation was performed against the constant load change rate process shown in Fig. 28**(a),** with the same average load change rate applied to both methods. Temperature, stress, and damage variations were compared between the two regulation strategies as the system load was ramped up from 25% to 100%.

As shown in Fig. 29**,** compared to the constant load change rate strategy, the proposed quadratic-function-based method reduces both the temperature and stress in the cooling wall throughout the load-increasing process. At the mid-process time of 600 s, the temperatures at points A, B, C, and D under the new strategy are reduced by 8.86 K, 2.12 K, 10.51 K, and 3.98 K, respectively. Correspondingly, the stresses are reduced by 15.91 MPa, 10.61 MPa, 21.53 MPa, and 11.26 MPa, respectively.

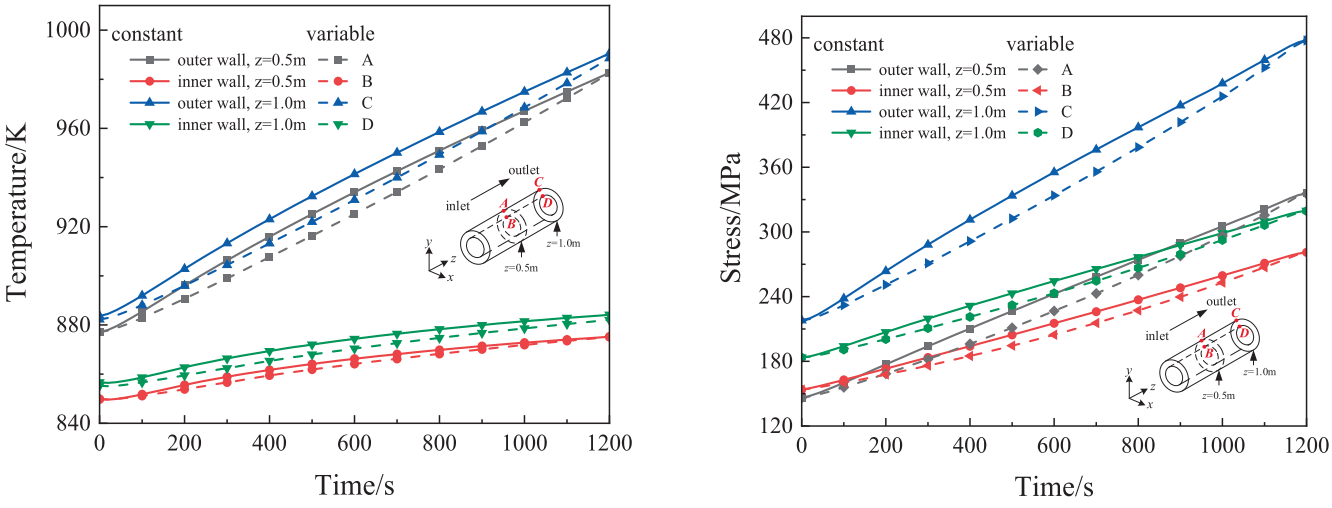
The quadratic-function-based method also effectively reduces both creep and fatigue damage compared to the constant-rate strategy (as shown in Fig. 30). At the mid-process time of 600 s, the creep damage values at points A, B, C, and D under the new strategy are reduced by 3.73×10^{-8}, 1.39×10^{-8}, 3.97×10^{-6}, and 8.22×10^{-7}, respectively. Similarly, the fatigue damage values are reduced by 1.98×10^{-7}, 3.16×10^{-8}, 3.67×10^{-6}, and 1.72×10^{-7}, respectively. Most significantly, at point C (the location of peak damage), the new control strategy reduces the maximum creep damage and the maximum fatigue damage by 37.56% and 27.45%, respectively, during the load-increasing process.

Fig. 31 illustrates the impact of load change control strategies on the cumulative damage in the cooling wall during the load-increasing process. When the unit operates at high loads, the cooling wall experiences



(a) Linear load increase in linear function form (b) Quadratic load increase in quadratic function form

Fig. 28. Variable load control method



(a) Temperature Comparison of Two Methods (b) Stress Comparison of Two Methods

Fig. 29. Effect of variable load regulation mode on temperature and stress distribution

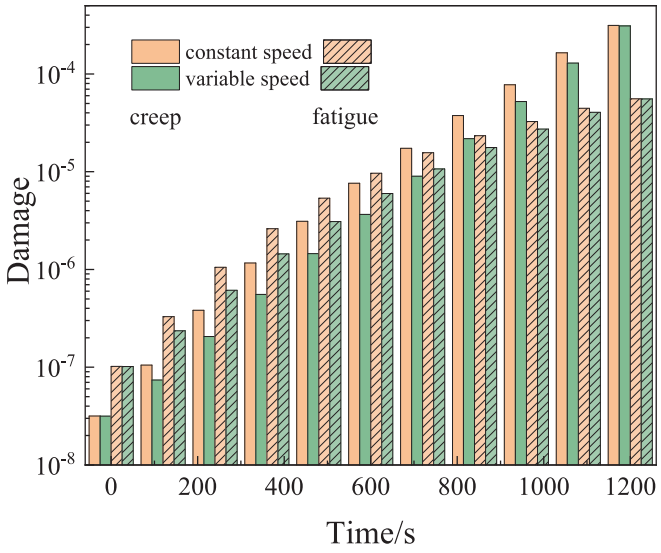


Fig. 30. Effect of load regulation mode on damage distribution

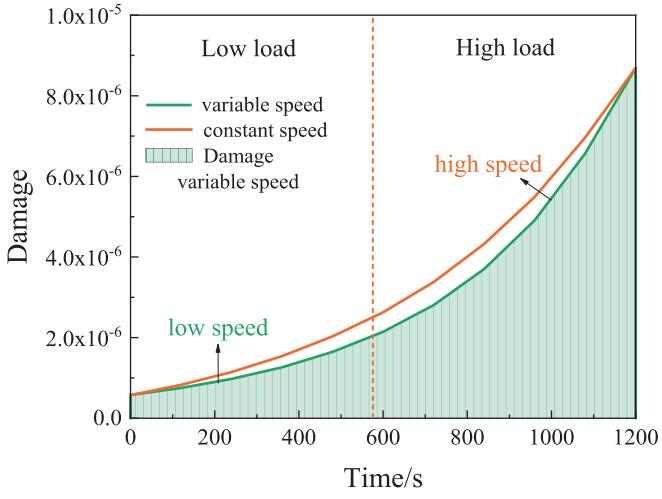


Fig. 31. Effect of load regulation method on the cumulative damage of cooling wall tubes

high temperatures and stresses. Employing a smaller load change rate in

this region prolongs exposure to these conditions, increasing the area under the damage-time curve and worsening cumulative damage. Conversely, a larger load change rate at high loads shortens residence time in this critical zone, effectively reducing cumulative damage. In the low-load region—characterized by lower temperatures and stresses where fatigue damage dominates — a larger load change rate would cause a faster temperature change, significantly increasing fatigue damage and the risk of transient damage. Thus, during load increases, a "higher rate at high load, lower rate at low load" strategy minimizes the coupled time integral of stress and temperature across the transient, effectively reducing overall cumulative damage to the cooling wall.

5. Conclusions

This study systematically investigates the comprehensive performance of S-CO_2 cooling wall tubes under variable-load peak-shaving operations. A steady-state three-dimensional multiphysics coupled model and a transient damage model are developed and validated against experimental data and theoretical analysis. The coupled fatigue–creep damage mechanisms of S–CO_2 cooling wall tubes under variable–load conditions were identified; a matching control strategy for heat flux and mass flux was proposed; and a quadratic–function–based load–rate matching strategy was developed, which effectively reduces temperature, stress, and damage. The primary contributions are summarized as follows:

(1) The distributions of temperature, stress, and damage within the cooling wall are obtained under both steady-state and transient variable-load conditions. The location of the maximum von Mises equivalent stress is load-dependent, shifting from the outer wall under high-load conditions to the inner wall under low-load conditions. Both fatigue and creep damage increase with rising wall temperature, with creep damage exhibiting a more rapid increase. A quantitative transition from fatigue-dominated to creep-dominated damage is identified: fatigue damage prevails at low loads, whereas creep damage becomes the dominant factor at high loads.

(2) The load change rate exerts a significant influence on cooling wall performance. When the load change rate increases from 2%/min to 6%/min under typical operating conditions, the maximum change rate of the maximum radial temperature difference and von Mises equivalent stress can rise approximately threefold. Meanwhile, creep damage increases by 31.3 times and fatigue damage by 22.4 times.

(3) A sensitivity analysis is conducted to evaluate the influence of key operating parameters, revealing that heat flux has a greater impact on cooling wall performance than mass flux. A matching law for heat flux and mass flux during load changes is proposed: during load reduction, with mass flux change rate set at 4%/min, heat flux change rate should be 5% higher; during load increase, with heat flux change rate set at 4%/min, mass flux change rate should be 2% higher. Application of this matching law throughout the entire load-variation process can effectively reduce the maximum temperature, fatigue and creep damage.

(4) An optimization strategy is proposed in which a quadratic function is employed to define the load change rate as a function of the system load. Compared with the constant-rate strategy, the proposed method effectively reduces the temperature rise rate of the cooling wall. During the load-increasing process, it achieves maximum reductions of 10.51 K in temperature and 21.53 MPa in stress, while reducing maximum creep damage by 37.56% and maximum fatigue damage by 27.45%.

The proposed strategy enhances operational flexibility and cooling-wall safety, thereby providing theoretical support for the optimized design of efficient S–CO_2 systems under transient variable-load conditions. However, the present study assumes a direct proportionality between heat flux and mass flux with plant load, which neglects the real-time evolution of heat flux during load transients, particularly owing to flame deflection at extremely low loads. To overcome this limitation, future work will develop a coupled combustion kinetics and transient heat transfer model for more accurate predictions of non-uniform heat flux evolution and its impact on cooling-wall safety. Additionally, beyond the current focus on heat flux–mass flux matching, subsequent research will also address system-level dynamic coordinated control that incorporates key parameters such as temperature and pressure.

CRediT authorship contribution statement

Ting Zhao: Writing – original draft, Visualization, Validation, Software, Project administration, Methodology, Formal analysis, Data curation, Conceptualization. **Yanjuan Wang:** Supervision, Project administration, Funding acquisition, Conceptualization. **Xuan Xu:** Visualization, Software, Investigation. **Junhao Cui:** Validation, Project administration, Investigation, Data curation. **Binhui Yu:** Visualization, Validation, Software, Conceptualization. **Jinliang Xu:** Validation, Supervision, Resources, Funding acquisition.

Declaration of competing interest

The authors declare that they have no known competing financial interests or personal relationships that could have appeared to influence the work reported in this paper.

Acknowledgements

The authors appreciate the financial support provided by the National Key Research and Development Program of China (No. 2023YFB4102202).

Data availability

Data will be made available on request.

References

[1] Wu C, Wang C, Hou Z, Wang Z. Flexible peak shaving in coal-fired power plants: A comprehensive review of current challenges, recent advances, and future perspectives. Energy 2025;138:0360–5442.
[2] Liao G, Liu L, Zhang F, Chen J, et al. Effects of technical progress on performance and application of supercritical carbon dioxide power cycle: A review. Energy Conversion and Management. 2019;199:111986.
[3] Crespi F, Gavagnin G, Sánchez D, Martínez GS. Supercritical carbon dioxide cycles for power generation: a review. Applied Energy, 2017;195:152–183.
[4] Ahn Y, Bae SJ, Kim M, Cho SK, Baik S, Lee JI, et al. Review of supercritical CO_2 power cycle technology and current status of research and development. Nuclear Engineering and Technology 2015;47:647–61.
[5] Guo J, Li M, He Y, et al. A systematic review of supercritical carbon dioxide(S-CO_2) power cycle for energy industries: technologies, key issues, and potential prospects. Energy Conversion and Management 2022;258:115437.
[6] Reznicek EP, Hinze JF, Rapp LM, et al. One-dimensional, transient modeling of a fixed-bed regenerator as a replacement for recuperators in supercritical CO_2 power cycles. Energy Conversion and Management. 2020;218:112921.
[7] Alison TC, Pelon MJ, R,, et al. Fundamentals and application of supercritical carbon dioxide based power cycles. Turbomachinery Cambridge: Woodhead Publishing; 2017. p. 147–215.
[8] Li H, Zhang Y, Bai W, et al. Control strategies and dynamic experimental tests on the wide-range and rapid load regulation of a first pilot multi-megawatts fossil-fired supercritical CO_2 power system. Energy Conversion and Management 2023;279:116748.
[9] Liu C, Xu J, Li M, et al. The comprehensive solution to decrease cooling wall temperatures of sCO_2 boiler for coal fired power plant. Energy 2022;252:124021.
[10] Yang Y, Bai W, Wang Y, et al. Coupled simulation of the combustion and fluid heating of a 300 MW supercritical CO_2 boiler. Applied Thermal Engineering 2017;113:259–67.
[11] Zhou J, Xiang J, Su S, et al. Key issues and practical design for cooling wall of supercritical carbon dioxide coal-fired boiler. Energy 2019;186:115834.
[12] Zhou J, Zhu M, Xu K, et al. Key issues and innovative double-tangential circular boiler configurations for the 1000 MW coal fired supercritical carbon dioxide power plant. Energy 2020;199:117474.
[13] Wan Z, Fang J, Tu N, et al. Numerical study on thermal stress and cold startup induced thermal fatigue of a water/steam cavity receiver in concentrated solar power (CSP) plants. Solar Energy 2018;170:430–41.

[14] Chen Y, Zhang Y, Wang D, et al. Effects of design parameters on fatigue-creep damage of tubular supercritical carbon dioxide power tower receivers. Renewable Energy 2021;176:520–32.
[15] Pitchumani,R, Nithyanandam, et al. Thermal and structural investigation of tubular supercritical carbon dioxide power tower receivers. Solar Energy, 2016; 135:374-385.
[16] Ortega J, Khivsara S, et al. Coupled modeling of a directly heated tubular solar receiver for supercritical carbon dioxide Brayton cycle: Structural and creep-fatigue evaluation. Applied Thermal Engineering 2016;109:970–8.
[17] Wang Y, Yu B, Gao S, et al. Performance Analysis of Cooling Wall of Supercritical CO_2 Coal-Fired Plants. Journal of Thermal Science 2022;31(6):1881–90.
[18] E.W. Lemmon, M.L. Huber, M.O. McLinden. NIST Standard Reference Database 23, Reference Fluid Thermodynamic and Transport Properties (REFPROP), version 9.0, National Institute of Standards and Technology. File dated December, 22: 2010.
[19] Wang K, Zhang Z, Li M, Min C. A coupled optical-thermal-fluid-mechanical analysis of parabolic trough solar receivers using supercritical CO_2 as heat transfer fluid. Applied Thermal Engineering 2021;183:116154.
[20] Chen Y, Wang D, Zou C, Gao W, Zhang Y. Thermal performance and thermal stress analysis of a supercritical CO_2 solar conical receiver under different flow directions. Energy 2022;246:123344.
[21] Lee YL, Barkey ME. Strain-Based Uniaxial Fatigue Analysis. Metal Fatigue Analysis Handbook. 2012:215–52.
[22] Wang Y, Wang B, Chen L, Materials. High-temperature low-cycle fatigue behavior of 625 nickel-base superalloy welding joint. Applied Mechanics & Materials, 2014; 618:120-124.
[23] Mao J, Tang D, Bao S, et al. High temperature strength and multiaxial fatigue life assessment of a tube sheet structure. Engineering Failure Analysis 2016;68:10–21.
[24] Gentile G, Picotti G, Binotti M, et al. Dynamic thermal analysis and creep-fatigue lifetime assessment of solar tower external receivers. Solar Energy 2022;247: 408–31.
[25] Morrow J. Cyclic plastic strain energy and fatigue of metals. PA: ASTM International West Conshohocken; 1965.
[26] Gonźalez-Ǵomez, P.A., Rodríguez-Śanchez, M.R., Laporte-Azcúe, M., Santana, D. Calculating molten-salt central-receiver lifetime under creep-fatigue damage. Solar Energy, 2021; 213:180–197.
[27] Laporte-Azcúe, M., Gonźalez-Ǵomez, P.A., Rodriguez-Sanchez, M.R., Santana, D. Deflection and stresses in solar central receivers. Solar Energy. 2020;195, 355-368.
[28] Shi C, Li R, Yang Z, et al. Heat transfer characteristics of boilers with different loads for 1000 MW coal-fired power units. Power Generation Technology. 2019;40(3): 213–9.
[29] Hedrick K, Hedrick E, Omell B, Zitney SE, Bhattacharyya D. Dynamic modeling, parameter estimation, and data reconciliation of a supercritical pulverized coalfired boiler. Industrial & Engineering Chemistry Research 2022;61:16764–79.
[30] Liu K, Wang C, Wang L, Liu B, Ye M, Guo Y, et al. Dynamic performance analysis and control strategy optimization for supercritical coal-fired boiler: a dynamic simulation. Energy 2023;282.
[31] Zhu B, Xu J, Wu X, Xie J, Li M. Supercritical “boiling” number, a new parameter to distinguish two regimes of carbon dioxide heat transfer in tubes. International Journal of Thermal Sciences 2019;136:254–66.
[32] Dewa RT, Park JH, Kim SJ, et al. High-temperature creep-fatigue behavior of Alloy 617. Metals 2018;8(2):103.
[33] Wang Y, Gao S, Shi W, et al. A novel structure tube for supercritical CO2 turbulent flow with high non-uniform heat flux. International Journal of Heat and Mass Transfer 2023;213.